All-in-one rheometry and nonlinear rheology of multicellular aggregates

Gaëtan Mary, François Mazuel, Vincent Nier, Florian Fage, Irène Nagle, Louisiane Devaud, Jean-Claude Bacri, Sophie Asnacios, Atef Asnacios, Cyprien Gay, et al.

All-in-one rheometry and nonlinear rheology of multicellular aggregates

Gaëtan Mary[1*], François Mazuel[1*], Vincent Nier[2], Florian Fage[1], Irène Nagle[1], Louisiane Devaud[1], Jean-Claude Bacri[1], Sophie Asnacios[1,3], Atef Asnacios[1], Cyprien Gay[1], Philippe Marcq[2,4], Claire Wilhelm[1†] and Myriam Reffay[1†]

[1] *Laboratoire Matière et Systèmes Complexes, UMR 7057, CNRS and Université de Paris Cité, 75205 Paris cedex 13, France*

[2] *Laboratoire Physico Chimie Curie, UMR 168, CNRS, Institut Curie, PSL University, Sorbonne Université, 75005 Paris, France*

[3] *Faculty of Science and Engineering, UFR 925 Physics, Sorbonne Université, Paris France*

[4] *Laboratoire Physique et Mécanique des Matériaux Hétérogènes, CNRS, ESPCI Paris, PSL University, Sorbonne Université, Université de Paris Cité, 75005 Paris, France*

* *These authors contributed equally to this work. and*

† *Corresponding author:* myriam.reffay@u-paris.fr

(Dated: March 22, 2022)

Tissues are generally subjected to external stresses, a potential stimulus for their differentiation or remodelling. While single-cell rheology has been extensively studied leading to controversial results about non linear response, mechanical tissue behavior under external stress is still poorly understood, in particular the way, individual cell properties translate at the tissue level. Herein using magnetic cells, we were able to form cellular perfectly monitored aggregates (magnetic molding) and to deform them under controlled applied stresses over a wide range of timescales and amplitudes (magnetic rheometer). We explore the rheology of these minimal tissue models using both standard assays (creep and oscillatory response) as well as an innovative broad spectrum solicitation coupled with inference analysis thus being able to define in a single experiment, the best rheological model. We find that multicellular aggregates exhibit a power-law response with non-linearities leading to tissue stiffening at high stress. Moreover we reveal the contribution of intracellular (actin network) and intercellular components (cell-cell adhesions) in this aggregate rheology.

INTRODUCTION

Mechanical behavior of biological tissues governs various processes ranging from developmental biology to cell migration or tumor invasion [1–6]. Biological tissues are complex 3D multicellular, heterogeneous and active materials [7]. Their intrinsic complexity makes them challenging to characterize as this necessarily entails to perfectly control and reproduce the tissue microscopic and macroscopic architecture. In this context, multicellular aggregates are highly relevant models of biological tissues for quantitative exploration [8, 9]. Organized in three dimensions and usually composed of a single cell type, their cell number, cell-cell interactions, and overall size are well-controlled. They allow one to decouple mechanics from genetic regulation. All these features make them simple, fully-controlled systems of choice, as testified by their widespread current use in developmental biology [10], organogenesis, tumorigenesis [11, 12], drug screening and biophysical research [12–15].

Single cells are the basic units of multicellular aggregates, their mechanics generally follow a scale-free power-law rheology at short time scale (from 10^{-5} to 10^{2} s) [16–21]. Many different techniques dedicated to determine the mechanical features of living cells [22] evidence this remarkable dynamical behavior. This power-law behaviour ousts the spring-dashpot models to impose the image of a cell with no dominating timescale [16] but rather characterized by a continuum of relaxation times and processes. Single cells are thus characterized by two parameters: the prefactor and the exponent of the power law. The prefactor quantifies the overall stiffness of the cell (its typical modulus), while the power-law exponent indicates the relative contributions of elastic (energy storage) and viscous-like (dissipation) behaviors. For single cells, the typical moduli are hundreds of Pascals while the exponent α is found in the range $0.15 - 0.3$, thus closer to an elastic solid ($\alpha = 0$) than to a viscous liquid behavior ($\alpha = 1$). Both depend on the level of applied stress, with evidence of stress-stiffening [23, 24] as well as of stress-softening [20], with attempts made to reconcile the two opposite observations [25].

In model tissues, behaviors operating on different timescales have been noticed [26]: elastic on short times scales (seconds to minutes) [27] where the tissue undergoes short-term reversible deformations proportional to the load, then visco-elastic on longer time scales (minutes to hours) [28–32] when cellular reorganization occurs. The relaxation time of fluctuations, on the order of 5 hours for F9 cells aggregates [33] was invoked for the transition between the two regimes. For longer time scales (days) cell division and death may also contribute to tissue fluidization [34]. The viscoelastic description sometimes extended to elasto-visco-plasticity characterizes model tissues by their surface tension, their Young's modulus, their viscosity and their yield stress. Many studies were dedicated to measure these long-time mechanical properties of multicellular aggregates. In contrast, the short-time mechanical behavior was not so fully examined while being at the center of single cell mechanics measurements. The rheology of multicellular aggre-

gates certainly depends on cell-scale mechanical properties but it should also be influenced by the mechanical properties of intercellular junctions [35] which exhibit viscoelastic properties [36]. However the link between cellular and junctional contributions is not straightforward [37]. While power-law reveals as describing both suspended monolayers [38, 39] or organs [40, 41], understanding how cell-scale mechanical properties (power law rheology, stiffness, non linearities) are translated at the collective scale remains an open question [42] as well as the respective contributions of the intracellular and intercellular components.

Moreover, the most common protocols to measure rheological properties of materials or cells are either the creep and recovery test which measure material deformation in response to a stress step application or the oscillatory experiments to look at possible frequency effects. Non linearities detection requiers to vary the amplitude of the stimulation thus having to repeat the experiments. New protocols based on large amplitude broad spectrum signals have been proposed but they have not been tested yet. On the experimental side, one major hurdle stems from the difficulty to apply controlled stress solicitations to designed minimal model tissues and to accurately measure their resulting deformations as well as from a lack of analysis tools. Herein we investigate the rheology of multicellular aggregates of F9 cells, a cell type which has been extensively studied both at the individual [21] and at the multicellular scale [8, 30, 33]. This was done thanks to an original all-in-one rheometer combining two important features: first, the ability to generate controlled cellular aggregates guaranteed by magnetic molding; second, to apply a wide range of stimulations both in terms of frequency and amplitude. Using this new setup, we could of course subject magnetic aggregates to standard rheological tests, but we could also introduce an original broad-spectrum stimulation to obtain, *in a single experiment* the best rheological model describing aggregate rheology. Besides, we tested the interplay between cell-scale mechanics and tissue-scale rheology. These protocols were cross-validated using a micro-plate rheometer specifically adapted to multicellular aggregates. Overall, the results demonstrate that multicellular aggregates exhibit a power-law rheological behaviour with stress-stiffening. Surprisingly, the stiffness of this cohesive cell assembly is lower than that of the corresponding individual cell. While cell-cell adhesion and individual cell stiffness do not affect the exponent governing the power law response, both contribute to the overall aggregate stiffness.

A MAGNETIC COMPRESSION RHEOMETER AT THE TISSUE SCALE

In order to quantify the rheological behavior of a multicellular aggregate, we stimulate this material mechanically with an arbitrary signal by remotely applying magnetic forces on all cells through internalized superparamagnetic nanoparticles [43]. Previous works have evidenced that incorporating magnetic nanoparticles does not modify neither the cell biological activity [44] nor their mechanical properties [45]. We further tested possible cytotoxicity effects on the F9 cells used in this work even under magnetic field exposure (Appendix A Methods) to discard harmfulness hypothesis, while apoptose is not detected in the aggregate (Figure 1-d). We use a magnetically inspired molding strategy [31] (Figure 1a and Appendix A Methods) to design multicellular aggregates of various shapes : cylinder (with a typical diameter of 2 mm and a height $h_0 = 1\,\mathrm{mm}$) as well as cuboid (1 mm long square base and 0.6 mm height). Whereas classical techniques (hanging drops, micro-wells or agitation) require several days to obtain spheroids of typically 500 nm diameter [33], magnetic molding yields within a single day to aggregates of various shapes and of millimeter-size. Obtained magnetic F9 cells aggregates are densily packed assemblies with an homogeneous cell density and structure of the cytoskeleton. Cells in these aggregates display well developed cell-cell adhesions (Figure 1d). The adhesions depend little on the radial position: a $20\,\mu$m-thick envelope after 24 h can be observed around a slightly less cohesive core.

These magnetically molded aggregates can be stimulated at will since the magnetic cellular force is generated by an electromagnet whose magnetic field is varied in a time-dependent manner. The magnetic field develops a tissue magnetization $M_V(B)$ and exerts a roughly constant pulling force $f_V = M_V(B)\,\frac{\mathrm{d}B}{\mathrm{d}z}$ per unit volume of aggregate (Figure 1 and Methods). The maximal exerted force is $2.2\,\mathrm{kN.m^{-3}}$. For z-independent sections (flat surface), no simple shear is induced and deformations are limited to uniaxial squeezing. The stress is always compressive, and we take a positive notation for simplicity. Its local value at any altitude z above the glass plate is simply given by the sum of all magnetic forces exerted on cells located higher within the aggregate: $\sigma_{\mathrm{loc}}(z) = \int_z^{h(t)} f_V(z')\,\mathrm{d}z'$. For a uniform volume force f_V, the stress increases linearly with the distance from its upper surface. We define σ as the spatially averaged value of the stress $\sigma \equiv \langle \sigma_{\mathrm{loc}}(z,t)\rangle_z$ in the magnetic rheometer which reduces to $\sigma = \frac{1}{2}\,h(t)\,f_V \approx \frac{1}{2}\,h_0\,f_V$. When $h_0 = 1\,\mathrm{mm}$, it reaches about 1 Pa for the maximal value of the applied magnetic field.

With this set-up (Figure 1g-h), the aggregate deformation varies in response to the compressive force imposed by the electromagnet, it does not exceed $\delta h \leq 50\,\mu\mathrm{m}$ meaning the overall aggregate strain is smaller than 5% for aggregates of a typical height $h_0 = 1\,\mathrm{mm}$.

In order to characterize the mechanical behavior of the aggregates, our aim is to measure the rheological response $\mathcal{R}$ relating the local strain $\varepsilon_{\mathrm{loc}}$ along the compression axis to the present and earlier values of the stress σ_{loc} along the same axis at the same location: $\varepsilon_{\mathrm{loc}}(z,t) = \mathcal{R}\left(\{\sigma_{\mathrm{loc}}(z,t'\}_{t'\leq t}\right)$. The magnetic rheometer provides the applied stress signal $\sigma(t)$ and the measured strain $\varepsilon(t) =$

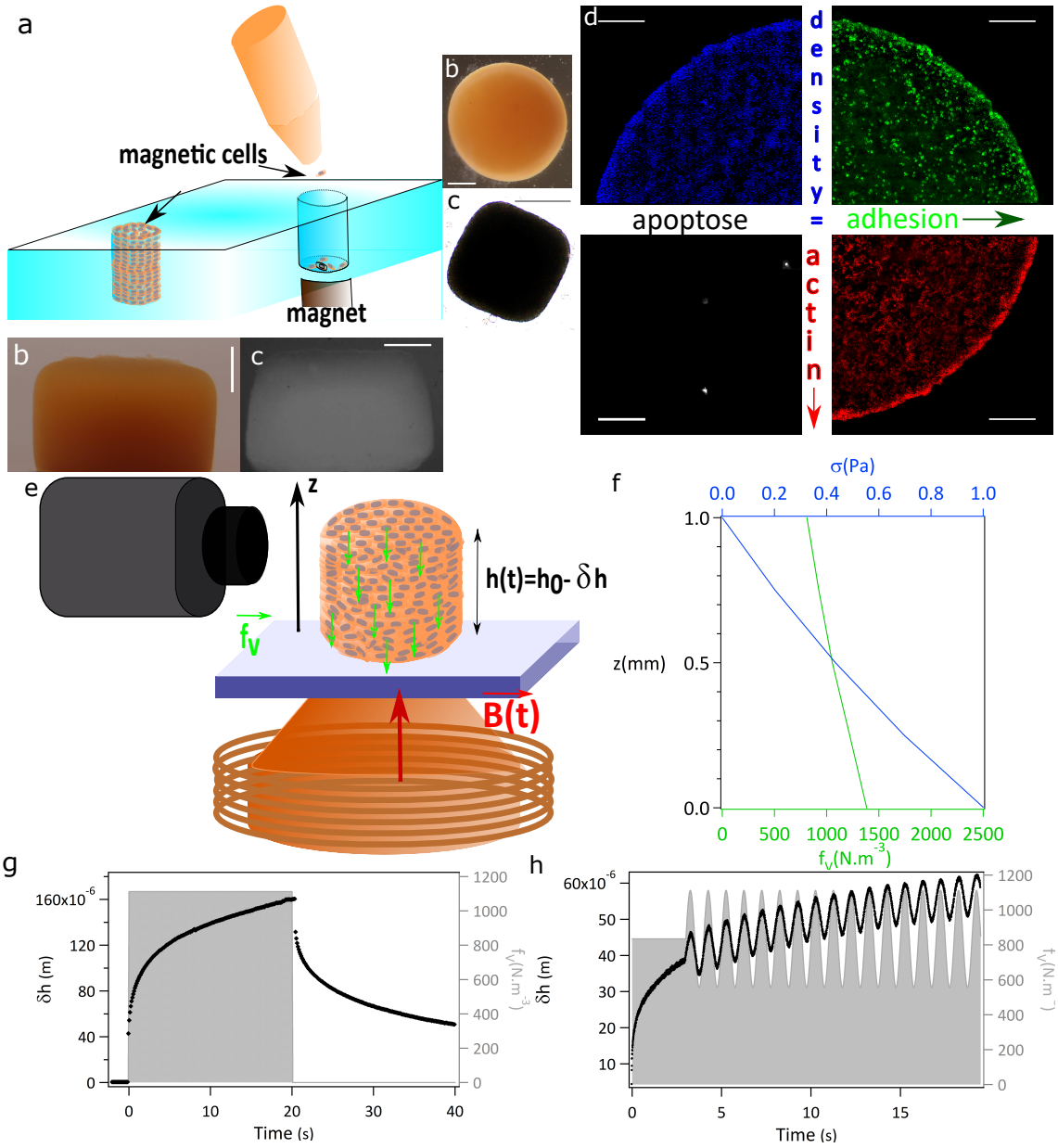

FIG. 1: **The magnetic rheometer. a** Schematics of the magnetic molding. Magnetic cells are seeded in an agarose well overhanging a magnet. Once the magnet has been removed cell-cell adhesions insure the cohesiveness of the assembly within a day.**b-c** Side and top views of magnetic multicellular aggregates. The magnetic molding technique provides the desired aggregate shape, here a cylindrical aggregate (**b**) or a cuboidal aggregate (**c**) (scale bar: 500 μm). **d** Quarter sections of a cylindrical aggregate stained with DAPI (blue), E-cadherin antibody (green), SiR-actin (red), and cleaved Caspase-3 antibody (white) (Scale bars: 100 μm). **e** Schematics of the magnetic rheometer. An aggregate is seeded in a 37°C thermostated tank filled with culture medium. Its sides are sealed with glass to allow fast camera imaging. An electromagnet composed of a central soft iron polar piece surrounded by a coil is positioned underneath to generate the magnetic field. The current supplied to the coil is delivered by an amplified signal generator. Imaging and magnetic signals are synchronized. **f** The force is almost constant over the aggregate height (less than 20% variation around the mean value f_V) while the stress increases approximately linearly with the distance from the top, with a mean stress value $f_V h_0/2$. **g-h** Magnetic forces per unit volume imposed to the whole aggregate (gray area) and measured deformation of the aggregate (black markers) are superimposed. The versatility of the rheometer allows to impose various signals, here a step (**g**) and a combination of a step with a superimposed 1 Hz sinusoid (**h**).

$\delta h(t)/h_0$ at the scale of the aggregate. The latter is equal to the spatial average of the local deformation, $\varepsilon(t) = \langle \varepsilon_{\rm loc}(z,t) \rangle_z$. Hence, assuming a linear local rheological response $\mathcal{R}$, it also relates directly the macroscopic strain

to the macroscopic applied stress: $\varepsilon(t) = \mathcal{R}\left(\{\sigma(t')\}_{t'\leq t}\right)$. (For the nonlinear regime, see Methods).

This set-up is highly versatile and aggregates can be subjected to various force signals: steps, ramps, sinusoidal and broad spectrum signals with frequencies ranging from 0.1 to 10 Hz (Figure 1g-h). Measurements were carried out on F9 murine embryonic carcinoma cells [46], a well-characterized cell line extensively studied both at the single cell level at short-time scale [19, 21, 47] and at the tissue level at longer time scale [30, 33]. F9 cell line is thus as a relevant model both to highlight collective effects at short-time scale and to allow comparison with behavior at longer time scale. Neverthless magnetic rheometry could be applied to other cell types, provided that the cells are able to form stable multicellular aggregates and have a sufficient magnetic potency based on endocytosis [43]. For instance, murine colon cancer cells CT26, have been successfully tested with the same protocol (Supplemental material).

POWER-LAW RHEOLOGY OF MULTICELLULAR AGGREGATES

We first use two classic signals: stress steps and single-frequency stress sinusoids.

The response to a force step signal of $1.1\,\mathrm{kN.m^{-3}}$, corresponding to a σ stepping up to $\sigma_0 = \frac{1}{2}\,h_0\,f_V = 0.55\,\mathrm{Pa}$ is recorded, (Supplemental Movie 1). Here, for $t \geq 0$ the applied stress is a constant, $\sigma = \sigma_0$. Hence, $\mathcal{R}$ is simply a function of time, and we define the function $J_{\sigma_0}(t)$ through: $\varepsilon_{\sigma_0}(t) \equiv \sigma_0\,J_{\sigma_0}(t)$. We observe (Figure 2a) that it coincides with a power-law function of time over four orders of magnitude (0.01 to 100 s):

$$J(t) = J_0\,(t/\tau)^{\alpha}, \tag{1}$$

Here we introduce the classical creep function $J(t)$, and drop the σ_0 subscript for J, assuming that the response is linear. The dimensional parameter τ is set to 1 s by convention.

Distributions of the exponent α and the prefactor J_0 are shown on figures 2b and c presenting their histograms and cumulative histograms (with J_0 in logarithmic scale) for 40 aggregates. The latter are fitted by an error function, yielding the average values as well as the standard deviation. We find $\alpha = 0.21 \pm 0.03$ (mean±sd) and $J_0 = (4.8 + 2.3, -0.9)\,10^{-2}\,\mathrm{Pa}^{-1}$ (mean±sd). Our sampling is consistent with normal and log-normal probability laws for α and J_0 respectively, in agreement with [18, 19]. As the dispersion between several measurements on a given aggregate is smaller than that observed between different aggregates, the magnetic rheometer is suitable to estimate the inherent distribution of rheological parameters. We checked that the measured rheological parameters are independent of aggregate's shape by comparing cylindrical and cuboid aggregates response (Supplemental material).

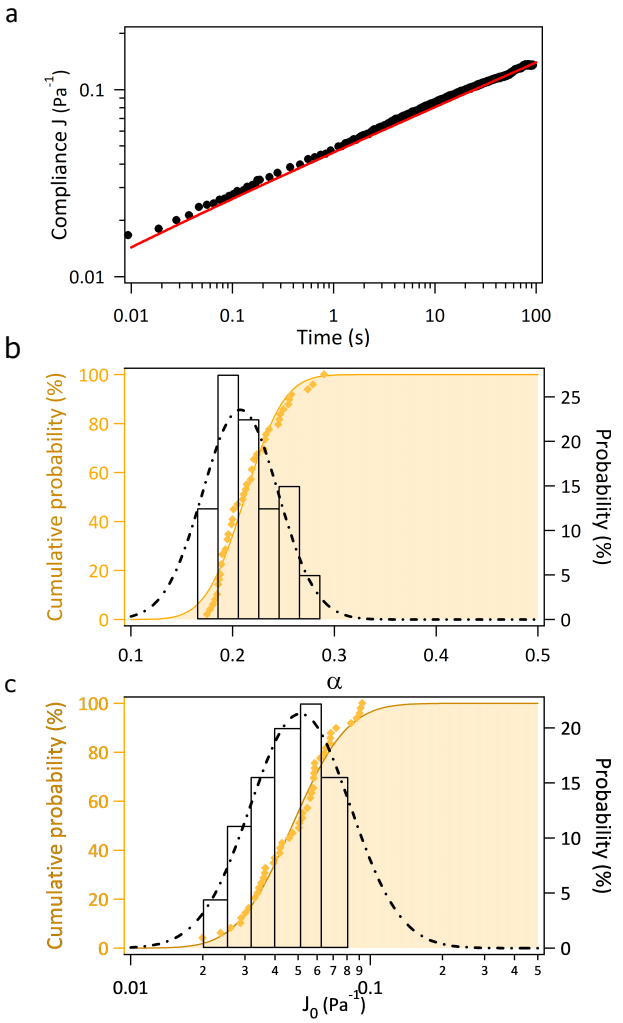

FIG. 2: **Creep function and power-law rheology. a** Creep function of a multicellular cylindrical aggregate submitted to a step of a $1.1\,\mathrm{kN.m^{-3}}$ force per unit volume, plotted in logarithmic scale. Experimental data (black crosses) are fitted with a power-law of time $J(t) = J_0\,(t/\tau)^{\alpha}$ with the measured exponent $\alpha = 0.21 \pm 0.03$ and compliance $J_0 = 0.048 \pm 0.015\,\mathrm{Pa}^{-1}$. **b-c** Cumulative distribution function (orange diamonds) and histogram (in black) of the exponent α (**b**) and of the compliance J_0 presented in logarithmic scale (**c**). The cumulative distribution functions of the exponent and of the logarithm of the compliance are fitted by an error function while their histograms are described by a normal distribution. Experiments were repeated over 55 different aggregates.

As the aggregate is stimulated in its linear regime, its deformation $\varepsilon(t)$ in response to an arbitrary imposed stress history $\sigma(t)$ can be expressed in terms of the above creep function. Indeed, the stress can be viewed as a series of stress steps $\mathrm{d}\sigma(t') = \frac{\mathrm{d}\sigma}{\mathrm{d}t}(t')\,\mathrm{d}t'$ at earlier times $t' \leq t$, and the deformation is expected to coincide with the sum of the corresponding creep functions:

$$\varepsilon(t) = \int_0^t J(t-t')\,\frac{\mathrm{d}\sigma}{\mathrm{d}t}(t')\,\mathrm{d}t' \tag{2}$$

To test the power-law response obtained with one step-like stress signal, we superimposed to it a sinusoidal force with amplitude $\sigma_{\rm osc}$ at angular frequency ω (corresponding to 3 Hz), starting a few seconds after the force step (Figure 3b). Eq. (2) predicts that in the linear regime, an oscillatory stress yields a sinusoidal strain response with complex amplitude $\varepsilon^\star_{\rm osc} = J^\star(\omega)\,\sigma_{\rm osc}$, where:

$$J^\star(\omega) = \frac{1}{E^\star(\omega)} = \frac{J_0\,\Gamma(1+\alpha)}{(i\omega\tau)^\alpha} \qquad (3)$$

with $E^\star(\omega)$ the complex Young modulus and Γ the Euler gamma function. The measurements (Figure 3a,b,d) are consistent with the superposition of the earlier power-law response to a force step given by Eq. (1) and the oscillatory response at 3 Hz. It is thus possible to extract a complex modulus value $E^\star(\omega)$ for each tested angular frequency ω.

Figure 3d displays the amplitude $|E^\star|$ and phase shift φ of the complex modulus for several frequencies $\omega/(2\pi)$ ranging from 0.1 to 10 Hz. The amplitude exhibits a power-law dependence on frequency $|E^*| \propto \omega^\alpha$ over two orders of magnitude, while the phase shift φ appears independent of frequency, consistently with Eq. (3) which predicts $\varphi = \alpha\pi/2$. E_0 is defined as the amplitude at 1 Hz, *i.e.*, $E_0 = |E^\star(\omega = 2\pi/\tau)|$. It is related to J_0 through Eq. (3): $E_0\,J_0 = (2\pi)^\alpha/\Gamma(1+\alpha)$. The oscillatory experiments yield $\alpha = 0.22 \pm 0.02$, hence $(2\pi)^\alpha/\Gamma(1+\alpha) \approx 1.64$, and $E_0 = 40 \pm 6\,$Pa, which corresponds to $J_0 = (4.2 \pm 1.0)\,10^{-2}\,\mathrm{Pa}^{-1}$. The result from the oscillatory regime is thus in good agreement with the one from the creep experiment. We extend the agreement between this two rheometry protocols from single cell [19] to the multicellular scale.

BACK-TO-BACK COMPARISON WITH A PARALLEL-PLATES RHEOMETER

As a cross-validation, we used a set-up initially designed for single-cell rheology [48], the parallel-plates rheometer [49], and extended it to the scale of multicellular aggregates. In their principle, measurements on cellular aggregates are similar to measurements on single cells. A cuboid aggregate is compressed between two glass microplates, a rigid one and a flexible one whose stiffness has been previously calibrated. Knowing the force applied to the cellular aggregate and its deformation, its compression viscoelastic modulus is estimated. The design of the flexible glass microplate (the force probe) had to be adapted specifically: while aggregates are far larger (around 500 μm radius) than single cells, they are softer (Figure 3d). Thus, original spatula-like plates with wide tips (1 mm in width) and a thin neck around 5 mm long and 100 μm width) were designed to reach a typical stiffness of tens of nN/μm (Methods). The sinusoidal stimulations exerted with the parallel-plates rheometer closely paralleled those exerted with the magnetic rheometer: aggregates were first compressed, then an oscillatory deformation in the $1-2\,\%$ range was applied. Studying the response of 7 cuboid aggregates, we find the same power-law rheology, characterized by an exponent $\alpha = 0.27 \pm 0.04$ and an elastic modulus $E_0 = 45 \pm 12\,$Pa. Quantitatively, cellular aggregates thus exhibit a slightly more prominent viscous-like component (higher α) than when tested with the magnetic rheometer, while estimates of the linear elastic modulus E_0 are consistent between the two instruments. This comparison corroborates the results obtained with the magnetic rheometer and confirms the power-law rheology of multicellular aggregates.

BROAD SPECTRUM RHEOLOGY

To systematically quantify aggregate rheology and its possible non-linearities in a single experiment, we introduce an original protocol in which we impose a large amplitude, broad spectrum stress signal (example on Figure 4a, see Methods for analytical expression and details). Magnetic rheometer is indeed highly versatile and allows for the application of designed stimulation signal. The rheological differential equation between strain and stress is inferred by identifying the relationship between their relevant times derivatives or integrals (Figure 4c,d). These signals and their time derivatives form a trajectory in the system phase space. Using a broad spectrum signal allows to explore the phase space efficiently and to thus sketch the manifold that corresponds to the constitutive equation.

Various, possibly non-linear, rheological models can be integrated over the altitude z, optimized to obtain the best parameter values in view of the experimental data, then compared quantitatively with each other (Methods). Inspired by the power-law creep linear response and by the litterature [50, 51], we tested a linear fractional model, and obtained a differentiation exponent $\alpha = 0.25 \pm 0.02$ and a compliance prefactor $J_0 = 0.045 \pm 0.010\,\mathrm{Pa}^{-1}$ ($N = 8$). It provides a fit with reasonable, yet far from perfect, quality (Figure 4b, blue line). Therefore, more general, nonlinear equations with one fractional element were investigated. Using the Akaike Information Criterion (Table I), we identify as the best model the following nonlinear fractional stress-strain relationship (Eq. (A3) in Methods):

$$\varepsilon_{\rm loc}(t) = J_1\; I^\tau_\alpha\left(\frac{\sigma_{\rm loc}(t)}{1+\sigma_{\rm loc}(t)/\sigma_{\rm c}}\right) \qquad (4)$$

where $I^\tau_\alpha(f(t))$ is the α-order fractional integral of the signal $f(t)$ [51]. Maximal likelihood optimization yields the following values of model parameters: the dynamical exponent $\alpha = 0.22 \pm 0.01$, the compliance $J_1 = 0.13 \pm 0.02\,\mathrm{Pa}^{-1}$ and the critical stress for non-linear effects $\sigma_{\rm c} = 0.5 \pm 0.1\,$Pa ($N = 8$). Note the good agreement between the value of the order of differentiation α and previous estimates obtained with classical rheological stimulations. Including either strain or stress thresh-

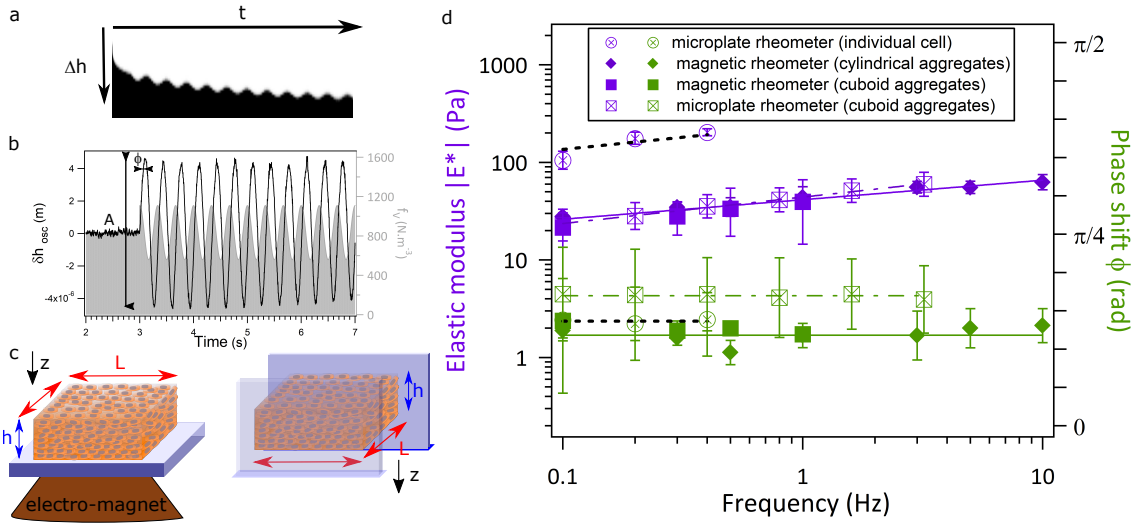

FIG. 3: **Harmonic regime and comparison with parallel plate rheology and single cell rheology. a** Kymograph of the upper interface of the aggregate submitted first to a force step of $834\,\mathrm{N.m^{-3}}$ and then to a force oscillation at a frequency of 3Hz and with an amplitude $280\,\mathrm{N.m^{-3}}$ around the step force. **b** Extracted oscillatory contribution of the deformation (in black) superimposed with the harmonic part of the applied force. Phase shift φ and amplitude A are measured at each frequency. **c** Respective geometries of the magnetic rheometer (left) and the parallel-plates rheometer (right). Cuboid aggregates are obtained by magnetic molding and form along z-axis. In the magnetic rheometer, the aggregates are compressed along their formation axis z while in the parallel-plates rheometer, aggregates are compressed along an orthogonal direction. **d** Frequency dependence of the modulus (purple symbols) and phase (green symbols) of the complex viscoelastic modulus E^* of the aggregates measured in two different geometries : cylinder (diamonds) and cuboid (squares) and with two distinct set-ups (magnetic and parallel-plates rheometers). Experiments were repeated for 45 cylindrical aggregates and 7 cuboid aggregates. Experimental data are fitted by a power-law for the modulus (purple lines) and by a constant for the phase shift (green lines) giving an exponent $\alpha = 0.22 \pm 0.01$ and a stiffness $E_0 = 40 \pm 6$ Pa for the magnetic rheometer. Results obtained with a single-cell microplates rheometer for F9 single cells loaded with nanoparticles (open circles) are included for comparison.

olds in the model did not improve agreement with experimental data, which ruled out the relevance of plastic behaviour [8] in the F9 multicellular aggregates in that range of deformations.

We next probe this non-linearity of the power-law response by applying bigger stress to the multicellular aggregate.

First a stress ramp $\sigma(t) = \dot{\sigma}_0\, t$ (where $\dot{\sigma}_0$ is a constant stress rate) is expected to generate a power-law response in the linear regime:

$$\varepsilon(t) = \frac{J_0\, \dot{\sigma}_0\, \tau}{(1+\alpha)} \left(\frac{t}{\tau}\right)^{1+\alpha} \qquad (5)$$

However the actual deformation (Figure 5a) shows an apparent deviation from this law for volume forces above $1.2\,\mathrm{kN.m^{-3}}$ (corresponding to 0.6 Pa stress when $h_0 = 1$ mm): the observed deformation is smaller than expected from Eq. (5). This stress stiffening is confirmed by recording the creep responses to different force steps corresponding to stress amplitudes ranging from 0.3 to 1.2 Pa. For each value of the stress, the creep deformation still follows a power-law with almost unchanged exponent (Figure 5c), while the compliance prefactor J_0 is reduced for higher stress levels (Figure 5d).

Eq. (4) also predicts strain histories when the aggregate is subjected to simpler stress signals. The creep response to a step stress solicitation is a single power-law function, as in the experimental observations, with a constant exponent α (Figure 5c) while the stress dependence of the estimated effective compliance reproduces the one established by step forcing (Figure 5d). Interestingly, an effective exponent that decreases with the applied force may be obtained by complementing the model with a second fractional integral acting on the strain (Eq. (A9) in Methods for additional details).

For each sample, a single broad spectrum experiment allowed us to recover the rheological features identified from stimulations based on both creep functions and harmonic signals and to generalize them in the form of a differential equation (Eq.4). Taken together, the analysis of all collected data confirms that the rheology of multicellular aggregates is best described by a fractional rheological law with a force-dependent prefactor (stress stiffening).

CONTRIBUTION OF SINGLE CELL MECHANICS

Since multicellular aggregates are essentially made of cells adhering to each other, their mechanical behavior is

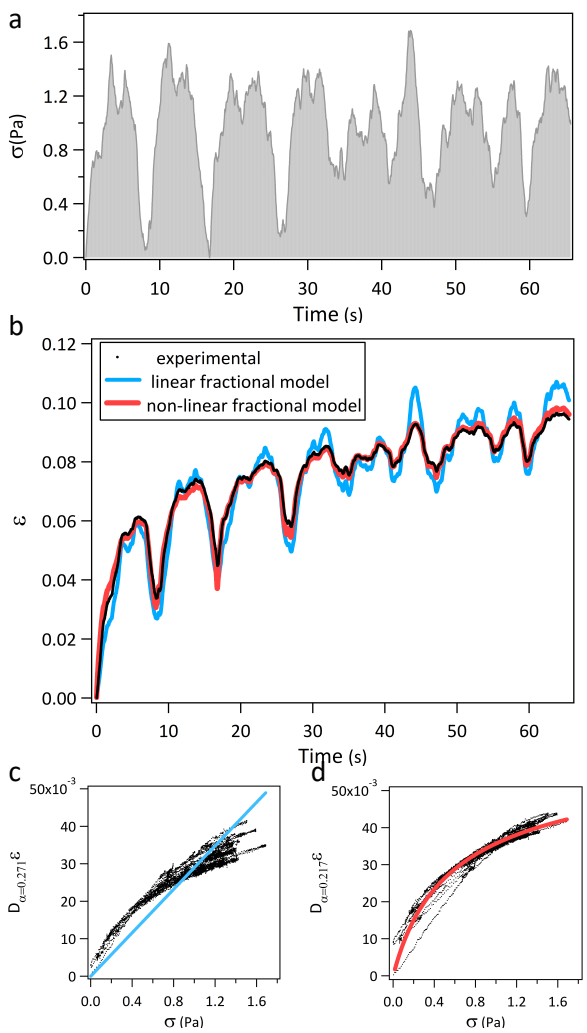

FIG. 4: **Broad spectrum rheology.** **a** Stress signal (grey) and **b** corresponding strain response of the aggregate (black points) fitted by different fractional models : linear power law model (blue curve), nonlinear fractional model defined by Eq. (A5) (red curve). **c-d** Phase space representation where the colored curves correspond to the functional form given by Eq. (A12) in the linear (blue) and nonlinear (red) fractional model. In respect with the use conventions, α-order derivatives of strain have the same dimension as the strain. Black points in all subfigures correspond to the same data. Differentiation exponents are different in **c** ($\alpha = 0.271$) and **d** ($\alpha = 0.217$) since their values were obtained by fitting different models to the same data set. The absolute fit quality is estimated by R^2-determination leading to an $R^2 = 0.94 \pm 0.02$ for linear fractional model and a $R^2 = 0.992 \pm 0.006$ for the non-linear fractional model (Eq. (A12))

expected to depend on the rheological properties of the individual cells as well as on cell-cell adhesion. To test these dependencies, we first investigate isolated F9 cells mechanical behavior.

We probe individual F9 cells in a single-cell microplate rheometer [48] (Figure 3d). Briefly, the applied deformation on individual F9 cells is in the $10 - 50\,\%$ range, and the elastic modulus is measured at different frequencies up to 0.5 Hz. The exponent found for F9 single cells ($N = 11$), $\alpha^{SC} = 0.27 \pm 0.03$, is consistent with the one measured in the microplate rheometer for F9 cell aggregates. Consistency between the two exponents is indeed expected as long as the time scale considered remains short compared to the typical cell rearrangement time [33], since cellular mechanical behavior is then expected to be predominant. However, F9 single cells are significantly stiffer than F9 cell aggregates, with an elastic modulus $E_0^{SC} = 240 \pm 80\,\mathrm{Pa}$, leading to $J_0^{SC} = (8 \pm 2)\,10^{-3}\,\mathrm{Pa}^{-1}$. Cellular behavior is not the only contribution of multicellular behavior mechanics even in this minimal tissue model.

At the single cell level α is less influenced by most inhibitors of cytoskeletal activity [20] than stiffness which appears as more sensitive. For instance latrunculin A (an inhibitor of actin polymerization) as well as blebbistatin (an inhibitor of actomyosin activity) softens the cells by 2 to 5-fold, depending on cell type and inhibitor concentration [16, 20, 52, 53]. This result is translated at the multicellular scale. On aggregates, latrunculin A disrupts the dense cortical actin meshwork visible in normal conditions: small patches with filaments no longer than $2\,\mu$m then appear (Figure 6d and e). Under control conditions, the typical actin filament length is $40 \pm 4\,\mu$m after 24 h maturation, of the order of the mean perimeter of the cells as actin is mainly cortical. This perimeter tends to increase with maturation time as cells became more hexagonal-like, and actin filament length reproduces these variations in the absence of latrunculin. Inhibitors effect is not reduced to the periphery of the aggregate but extends to the inner cells.
Quantitatively, the exponent α does not change drastically (Figure 6e), the slighlty more elastic behavior noticed under latrunculin A addition suggests that actin depolymerization does not necessarily makes the cells more dissipative as was already demonstrated [54, 55]. By contrast, a twice higher compliance (Figure 6f) is measured meaning aggregates become twice softer reproducing results obtained in single cells [20].
However because of the cross-talk between actin organization and cell-cell adhesion strength, we also examine cell contractility role by adding blebbistatin. Blebbistatin acts on myosin II by inhibiting ATP, it decreases the motor activity of the myosin but also modifies its attachment dynamics. At the reconstituted actin gel and at the single cell levels, its addition leads to a more elastic behavior (α exponent decrease) and a softening (decrease of the compliance) [53, 56]. This action is translated at the multicellular scale indeed we show up no impact on α exponent whereas slightly decreasing but an important decrease of the compliance. It thus reveals the impact of individual cells mechanics through actin disorganization and contractility on aggregates stiffness.

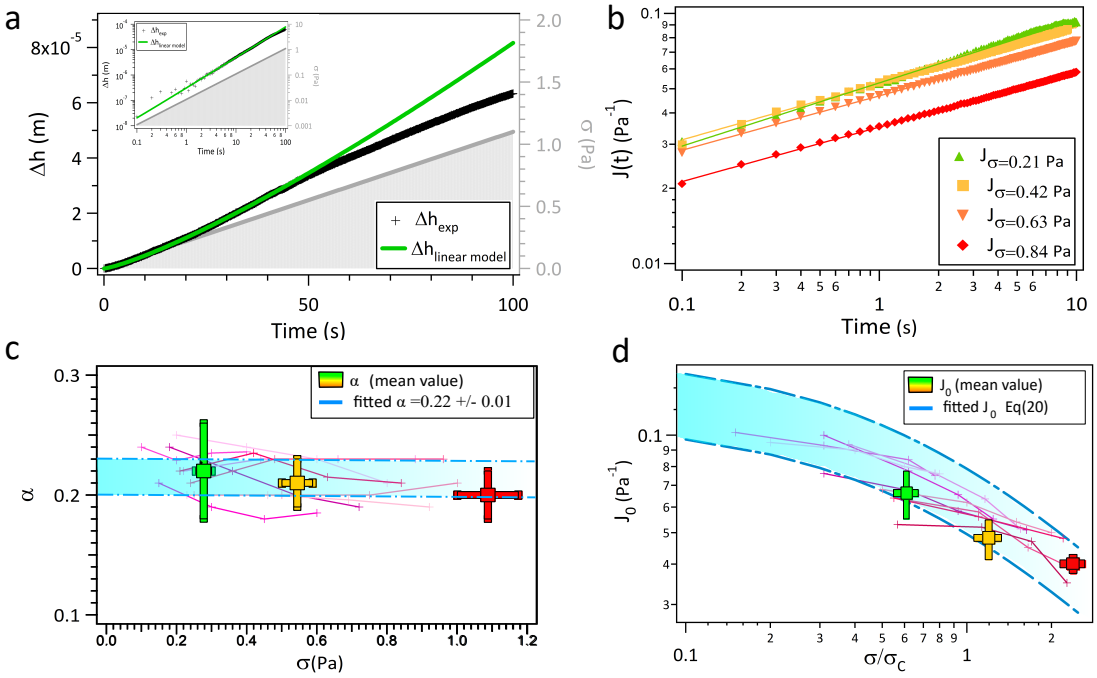

FIG. 5: **Non linearity of the rheological parameters. a** Displacement (black crosses) of the upper surface of the aggregate submitted to a stress ramp from 0 to 1.1 Pa in 100 s (grey signal). The expected linear answer is superimposed in green. The insert is a logarithmic scale zoom of the signal to emphasize the global $\alpha + 1$ exponent at small deformations. **b** Creep functions obtained for four different stress steps ($\sigma = 0.21, 0.42, 0.63, 0.84$ Pa). **c-d** Variation of the exponent α and the compliance J_0 with the stress. Mean data obtained from the independent creep experiments performed at 3 different stress levels with the applied stress ($\sigma = 0.27, 0.54$ and 1.1 Pa) are superimposed on individual data obtained from aggregates which have experimented four stress steps (pink curves). One has to pay attention to the fact that for J_0 variations, the discrepancies related to the individual variation of the critical stress σ_C are almost wiped out by fitting individually this parameter in the range $\sigma_C = 0.45 \pm 0.10\,\mathrm{Pa}^{-1}$. These results are compared with the nonlinear fractional model prediction delimited by the light blue area and corresponding to the possible range of stiffness extracted from broad range spectrum response fits.

CONTRIBUTION OF CELL-CELL ADHESION

We next examined the role of cell-cell adhesion in the mechanical properties of cell aggregates, first by varying the maturation time from 16 h to 48 h, second adding EGTA to inhibit the formation of intercellular adhesions. Indeed, increasing the maturation time leads to more cohesive aggregates: cell-cell adhesions develop with time from the periphery to the center of the aggregate (Figure 6a-b and Figure 6e). Conversely, under the action of EGTA, a calcium ion chelator decreasing intercellular adhesion forces without affecting single cell mechanical features [20], the aggregates appear looser, with a lower expression level of cadherins at the membrane (Figure 6c) and a decrease of E-cadherin mediated cell-adhesion length per cell (Figure 6e). In these conditions, while the exponent α is not significantly modified by the degree of intercellular adhesion (Figure 6f), the compliance factor J_0 depends on the cell-cell contacts (Figure 6g): when the aggregate cohesiveness is reduced, either by shortening the maturation time or under the action of EGTA, the aggregate becomes softer (larger value of J_0). Conversely, the maturation of cell-cell adhesions stiffens the aggregate and at 48 h of maturation, the compliance of the aggregate becomes remarkably close to the one of isolated F9 cells.

It may appear surprising that EGTA is not observed to fluidize the aggregate behaviour quantitatively but our experiments do not involve strong applied stresses [37]. Furthermore, experiments durations are too short to involve a significant number of spontaneous cell divisions or apoptosis and subsequent cell rearrangements, we correspondingly do not expect fluidization under weak applied stresses [34]. In the absence of complete cell rearrangements, the slight decrease of α upon addition of EGTA probably results from the combination of two antagonistic tendencies. On one hand, loosening cell-cell adhesion eases sliding motions between neighbouring cells and we expect it to correspondingly favour energy dissipation as opposed to storage, thus increasing α. On the other hand, loosened adhesion may ease aggregate compaction, whether spontaneous as already observed in aggregates [57] or due to the mechanical history as characterized in granular materials [58]. Such compaction should enhance the number and surface area of cell-cell contacts and thus reduce the chances of non-affine, dissi-

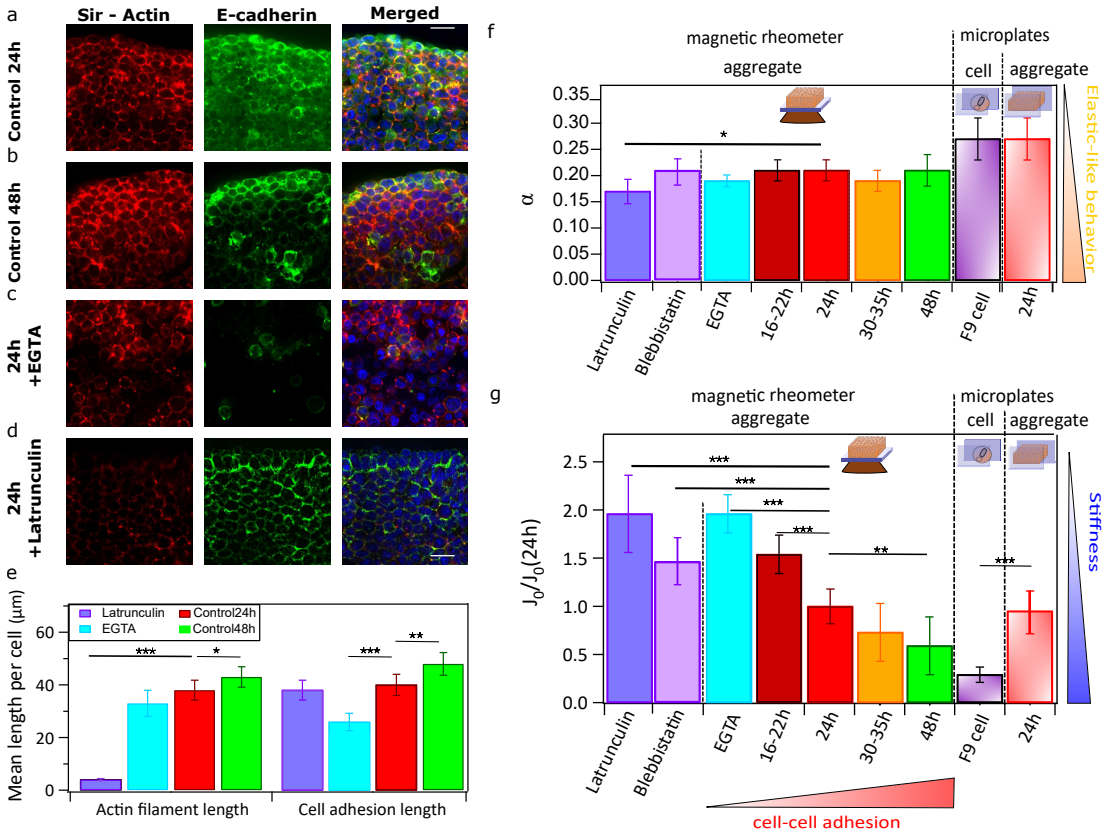

FIG. 6: **Contribution of cell-cell contacts and cell cytoskeleton on aggregates rheology. a-d** Immunofluorescence images of aggregates both in the center and on the periphery. Scale bars indicate 20 μm. Nuclei (DAPI labelling), cadherins (GFP E-cadherin antibody) and actin filaments (SiR-Actin) are labelled. **e** The mean length of F-actin fibers within a cell and of cadherin patches on the periphery of each cell are compared in each situation. Results are obtained from three independent samples per condition. Mann-Whitney tests are applied and significance are indicated when relevant ($\star$ stands for a significance degree p, $p < 0.01$, $\star\star$ for $p < 0.001$, $\star\star\star$ for $p < 0.0001$). **f-g** Impact of maturation time (from 16 to 48 hours), disruptive agents (EGTA, blebbistatin and latrunculin A) and depletion of α-catenin on the exponent α (**e**) and compliance (**f**), expressed in fold increase as compared to the value at 24 hours maturation time (light red), chosen as standard. The experiments have been carried out on independent replicates ($N > 20$ for EGTA and various maturation time, $N = 22$ for blebbistatin, $N = 44$ for latrunculin and $N = 51$ for 24 h hours maturation)). Mann-Whitney statistical tests are used to look at differences. When significant, these differences with the standard are indicated. Stars numbers indicate the degree of significance ($\star$ for $p < 0.01$, $\star\star$ for $p < 0.001$, $\star\star\star$ for $p < 0.0001$).

pative deformations, thus contributing to lowering the exponent α. The weak decrease of α observed when EGTA is used suggests that the latter phenomenon may possibly have a greater impact than the former.

DISCUSSION

An all-in-one magnetic rheometer for model tissues
Our work shows that magnetic cells may act as actuators to apply controlled internal forces on the aggregate they form. This allows to create an all-in-one rheometer combining aggregate formation (control of aggregate size, shape and content thanks to magnetic molding) with compressive versatile solicitation.

Two differents set-ups were designed and compared to determine the rheology of molded magnetic multicellular aggregates: the magnetic rheometer and the parallel-plate rheometer. Given that estimates of single cell rheological parameters often differ by orders of magnitude when measured by different techniques [22], the agreement between these two rheometers is remarkable and validates the internal magnetic rheometry method. Magnetic rheometry is thus able to test the rheology of model tissue.

So far two techniques have been dedicated to the rheology of multicellular aggregates or tissue extracts at short time scale: the shear rheometer [8] and relaxation compressive plates rheometry [27]. Shear rheometer by looking at numerous aggregates on a single experiment is highly precise however no absolute value can be extracted because of the difficulty to estimate surface contact. Compressive plates relaxation focused on a single aggregate but can not vary at will the stimulation type.

The magnetic rheometer overcomes these two limitations by looking at single aggregate rheology in compression and by proposing various simulation patterns.

The magnetic rheometer allows indeed to exert arbitrary compressive stress signals in the range from 0.1 to 10 Hz. It offers a unique opportunity to implement broad spectrum rheology, an approach which aims at providing the constitutive equation of the material using a single experiment per sample. This is reminiscent of the optimally windowed chirp protocol introduced in [59, 60], a protocol carried out in Fourier space. In contrast, the present broad spectrum protocol is performed in real space, thereby allowing to fully characterize nonlinearities with only one signal.

Multicontribution of cell-cell interaction and cellular rheology to multicellular aggregate rheology

The direct measurements of model tissue rheology reported here reveal that multicellular aggregates behave as viscoelastic materials well described by a nonlinear fractional model with stress stiffening. The nonlinear form given in (4) is reminiscent of the dependence found experimentally between stiffness and stress for single cells [21, 61]. It evokes the local surface tension reinforcement measured for cellular aggregates [29] at longer timescale, and may be the signature of an active response of cells to mechanical stress.

The creep function of the aggregate is a power law function. This behavior is the hallmark of the presence of a continuous distribution of relaxation times, first identified at the individual cell level [19]. The value of α close to 0.2 puts multicellular aggregates in the same range as individual cells in terms of dynamics. This dynamic exponent also proves robust to most perturbations. By contrast, stiffness is remarkably sensitive not only to intracellular cytoskeleton (reflecting the single cell rheology change in the case of latrunculin-A actin disruption, or myosin inhibition due to blebbistatin) but also to cell-cell adhesions. The compliance J_0 decreases (stiffening) as the aggregate matures (Figure 6). Indeed as cellular adhesions develop, individual cells become more sharply faceted, expulse interstitial fluid from the aggregate [57] and reduce their sliding possibilities in the interstitial regions. This change in geometry, as in liquid foams, corresponds to a stiffening of the entire structure since it increases the level of local deformations required to match a given macroscopic deformation. Alongside, we observed a softening (Figure 6) in the presence of EGTA, which is known to weaken cell-cell adhesion and results in less faceting cells. This dependence with the strength of cell-cell adhesion is remarkable as in this range of timescale (shorter than the fluctuation time measured around 5 hours for F9 cells [33] or the T1 transition time in tissue [62, 63]), cell rearrangements do not occur, meaning that the magnetic rheometer should be more sensitive to the intracellular modifications than the intercellular ones. The actual results imply that cell-cell adhesions are actually also tested through short time and small deformations. Single cells appear stiffer

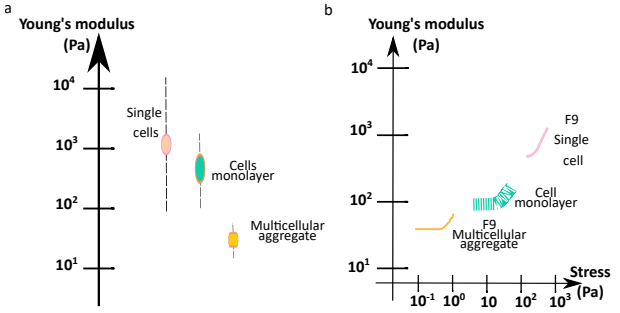

FIG. 7: **Stiffness and non linearities characteristics of cellular materials. a** Young's modulus of cellular materials and component starting single cells [61], cell monolayers [38] and multicellular aggregates (present study). Multicellular aggregates appear softer than any other cellular materials with a Young's modulus orders of magnitude below cell or actin. **b** Evolution of the Young's modulus with the magnitude of the applied stress for single cells, cell monolayer [64] and multicellular aggregates. Stress stiffening can be noticed at the three scale but exhibits different thresholds.

than the multicellular aggregates (Figure 3, Figure 7a), even after maturation up to 48 hours, (Figure 6f). First that may result from boundary conditions being very demanding in the single-cell experiment, where a significant fraction of the cell surface is connected to rigid plates and the cell has to largely deform. By contrast, in measurements on the entire aggregate, the overall deformation imposed can be reached through a combination of cell deformations modes since the surroundings of each cell is then softer. Note that this argument also applies to 2D situations, making 2D epithelia softer than single epithelial cells, as measured in a suspended geometry [65]. Multicellular aggregates are actually closer to the stiffness of the cytoplasm [66] or biopolymer diluted gels [67]. These deformations mode may thus implied either the cytoplasm or the cell-cell adhesions. Moreover the cells inside the aggregate experience a softer environment and may adapt to its stiffness as was already demonstrated on 2D substrates of varying stiffness [68, 69].

Finally, comparison between different inhibitors highlights that both intercellular and intracellular components contribute to the multicellular aggregates behavior even at short time scale.

Stress stiffening of cellular materials

Stress stiffening, observed here with cell aggregates, has previously been reported for complex polymeric materials as well as living cells [70–72] (Figure 7b). For polymers, alignment along the direction of the applied force leads to an increased resistance, which contributes to the stiffening of the network. This contribution, present at the scale of the cytoskeleton, may extend to the cellular, as well as to the multicellular scale. In tissues, cell-cell arrangements may also play a role as stress can disrupt adhesion

and facilitate in turn cell-to-cell movements leading to a stress softening. However, since maximal deformations in our experiments are in the 5% range, the disruption of cell junctions seems unlikely to be relevant but cell-cell junction elasticity as well as cell deformations may contribute. The stress stiffening arises above 1 Pa corresponding to 3% deformation. This threshold is much more important in single cells (around $10^2 - 10^4$ Pa [61, 73]) and in cell monolayers (several tens to hundreds Pa [38, 39, 64]) corresponding in both cases to deformation above 10%. The obtained threshold stress value is rather in the range of stress stiffening observed for cytoskeletal to extracellular proteins [67] and reconstituted actin networks [74] from 1 to 10 Pa. As small stresses are accessible with the magnetic rheometer, while most other techniques dedicated to single cells focus on larger stresses, a multi-step stress stiffening at different force levels may be implied. The threshold in the case of multicellular aggregate may be the signature of cell-cell interactions elasticity enhancing the sensitivity of the set-up.

CONCLUSION

Unsurprisingly, the rheology of multicellular aggregates presents similarities with single cell and cell monolayer rheology in spite of marked differences in terms of scales and structures. Indeed we find that their response to a step-compression follow a power-law in the range from tenths of seconds to minutes, with a comparable dynamical exponent. Moreover we shed light on the shared contribution of individual cell mechanics and cell-cell adhesion on model tissue rheology. Remarkably, cell mechanics modification as well as intercellular adhesion changes both impact aggregate stiffness thus cell mechanical properties and cell-cell adhesion strength translate at the multicellular level, and are captured by our original magnetic rheometer. However, the behaviour of multicellular aggregates differs from that of single cells. Their effective compliance is higher than that of single cells, and depends on the maturation of cell junctions. Besides multicellular aggregates exhibit stress stiffening above stresses of the order of 1 Pa in the range of observed biological gels stiffening threshold and clearly in the range of their actual elastic modulus. The adaptation of non linearities stress threshold range to elastic modulus range from the single cell level to the multicellular one is highlighted here.

The magnetic rheometer brings up the possibility to exert small forces and study precisely the small deformations of millimeter scale multicellular aggregates. It presents an enhance sensitivity able to look at molecular modification of intracellular or intercellular components. Together with model inference and model selection, broad spectrum analysis allows to decipher in a single acquisition the rheological model that best describes a sample. Thanks to its versatility both with respect to the nature of applied signals (from step to multi frequency force signal) and to the nature of biological samples (cell types, drugs and inhibitors), the all-in-one magnetic rheometer either on its own, or coupled with inference analysis could become a key player for the mechanical exploration of biological model tissues, and help elucidate which biochemical or physical factors affect multicellular aggregates rheology. For instance, the role played by secreted or artificially added extracellular matrix in the mechanics of model tissues could represent a challenging question to address in the future. In particular embryo morphogenesis not only arises from cell generated forces but also on tissues mechanical properties [75]. Being able to measure tissue deformation in response to stress modification should shed light on embryonic development mechanisms. Moreover as mechanical properties of tissues from the molecular to the macroscopic scale prove to be fundamental for tissue function and cell behavior, field of biomaterial development, tissue engineering and regenerative medecine have to integrate mechanics of living tissues to tackle challenges of engineering lifelike tissues.

[1] T. A. Engstrom, T. Zhang, A. K. Lawton, A. L. Joyner, and J. M. Schwarz, Buckling without bending: A new paradigm in morphogenesis, Phys. Rev. X **8**, 041053 (2018).

[2] V. M. Weaver, Cell and tissue mechanics: the new cell biology frontier, Molecular Biology of the Cell **28**, 1815 (2017).

[3] K. Sugimura, P.-F. Lenne, and F. Graner, Measuring forces and stresses in situ in living tissues., Development **143**, 186 (2016).

[4] O. Campàs, A toolbox to explore the mechanics of living embryonic tissues, Seminars in Cell & Developmental Biology **55**, 119 (2016).

[5] A. Mongera, P. Rowghanian, H. J. Gustafson, E. Shelton, D. A. Kealhofer, E. K. Carn, F. Serwane, A. A. Lucio, J. Giammona, and O. Campas, A fluid-to-solid jamming transition underlies vertebrate body axis elongation, Nature **561**, 401 (2018).

[6] A. Saraswathibhatla and J. Notbohm, Tractions and stress fibers control cell shape and rearrangements in collective cell migration, Phys. Rev. X **10**, 011016 (2020).

[7] N. Harmand, A. Huang, and S. Hénon, 3d shape of epithelial cells on curved substrates, Phys. Rev. X **11**, 031028 (2021).

[8] T. V. Stirbat, S. Tlili, T. Houver, J.-P. Rieu, C. Barentin, and H. Delanoë-Ayari, Multicellular aggregates: a model system for tissue rheology., Eur Phys J E Soft Matter **36**, 9898 (2013).

[9] J. Ackermann, M. B. Amar, and J.-F. Joanny, Multicellular aggregates, a model for living matter, Physics Reports **927**, 1 (2021).

[10] V. Du, N. Luciani, S. Richard, G. Mary, C. Gay,

F. Mazuel, M. Reffay, P. Menasché, O. Agbulut, and C. Wilhelm, A 3d magnetic tissue stretcher for remote mechanical control of embryonic stem cell differentiation, Nature Communications **8**, 10.1038/s41467-017-00543-2 (2017).

[11] R.-Z. Lin and H.-Y. Chang, Recent advances in three-dimensional multicellular spheroid culture for biomedical research, Biotechnology Journal **3**, 1172 (2008).

[12] S. Nath and G. R. Devi, Three-dimensional culture systems in cancer research: Focus on tumor spheroid model, Pharmacology and Therapeutics **163**, 94 (2016).

[13] X. Cui, Y. Hartanto, and H. Zhang, Advances in multicellular spheroids formation, Journal of The Royal Society Interface **14**, 20160877 (2017).

[14] A. A. Lucio, A. Mongera, E. Shelton, R. Chen, A. M. Doyle, and O. Campàs, Spatiotemporal variation of endogenous cell-generated stresses within 3d multicellular spheroids, Scientific Reports **7**, 10.1038/s41598-017-12363-x (2017).

[15] F. Pampaloni, E. G. Reynaud, and E. H. K. Stelzer, The third dimension bridges the gap between cell culture and live tissue., Nat Rev Mol Cell Biol **8**, 839 (2007).

[16] B. Fabry, G. N. Maksym, J. P. Butler, M. Glogauer, D. Navajas, N. A. Taback, E. J. Millet, and J. J. Fredberg, Time scale and other invariants of integrative mechanical behavior in living cells, Phys. Rev. E **68**, 041914 (2003).

[17] J. Alcaraz, L. Buscemi, M. Grabulosa, X. Trepat, B. Fabry, R. Farré, and D. Navajas, Microrheology of human lung epithelial cells measured by atomic force microscopy, Biophysical Journal **84(3)**, 2071 (2003).

[18] N. Desprat, A. Richert, J. Simeon, and A. Asnacios, Creep function of a single living cell, Biophysical journal **88**, 2224 (2005).

[19] M. Balland, N. Desprat, D. Icard, S. Féréol, A. Asnacios, J. Browaeys, S. Hénon, and F. Gallet, Power laws in microrheology experiments on living cells: Comparative analysis and modeling, Phys. Rev. E **74**, 021911 (2006).

[20] X. Trepat, L. Deng, S. S. An, D. Navajas, D. J. Tschumperlin, W. T. Gerthoffer, J. P. Butler, and J. J. Fredberg, Universal physical responses to stretch in the living cell., Nature **447**, 592 (2007).

[21] P. Kollmannsberger and B. Fabry, Linear and nonlinear rheology of living cells, Annu Rev Mat Res **41**, 75 (2011).

[22] P.-H. Wu, D. Raz-Ben Aroush, A. Asnacios, W.-C. Chen, M. Dokukin, B. Doss, P. Durand-Smet, A. Ekpenyong, J. Guck, N. Guz, P. Janmey, J. Lee, N. Moore, A. Ott, Y.-C. Poh, R. Ros, M. Sander, I. Sokolov, J. Staunton, N. Wang, G. Whyte, and W. G, A comparison of methods to assess cell mechanical properties, Nat Meth **15**, 491 (2018).

[23] V. Vogel and M. Sheetz, Local force and geometry sensing regulate cell functions., Nat Rev Mol Cell Biol **7**, 265 (2006).

[24] B. D. Matthews, D. R. Overby, R. Mannix, and D. E. Ingber, Cellular adaptation to mechanical stress: role of integrins, Rho, cytoskeletal tension and mechanosensitive ion channels., J Cell Sci **119**, 508 (2006).

[25] L. Wolff, P. Fernández, and K. Kroy, Resolving the stiffening-softening paradox in cell mechanics., PLoS One **7**, e40063 (2012).

[26] D. Gonzalez-Rodriguez, K. Guevorkian, S. Douezan, and F. Brochard-Wyart, Soft matter models of developing tissues and tumors., Science **338**, 910 (2012).

[27] M. Yu, A. Mahtabfar, P. Beelen, Y. Demiryurek, D. I. Shreiber, J. D. Zahn, R. Foty, L. Liu, and H. Lin, Coherent timescales and mechanical structure of multi-cellular aggregates, Biophysical Journal **114**, 652a (2018).

[28] A. Kalantarian, H. Ninomiya, S. M. I. Saad, R. David, R. Winklbauer, and A. W. Neumann, Axisymmetric drop shape analysis for estimating the surface tension of cell aggregates by centrifugation., Biophys J **96**, 1606 (2009).

[29] K. Guevorkian, M.-J. Colbert, M. Durth, S. Dufour, and F. Brochard-Wyart, Aspiration of biological viscoelastic drops., Phys Rev Lett **104**, 218101 (2010).

[30] T. V. Stirbat, A. Mgharbel, S. Bodennec, K. Ferri, H. C. Mertani, J.-P. Rieu, and H. Delanoë-Ayari, Fine tuning of tissues viscosity and surface tension through contractility suggests a new role for α-catenin., PLoS One **8**, e52554 (2013).

[31] F. Mazuel, M. Reffay, V. Du, J.-C. Bacri, J.-P. Rieu, and C. Wilhelm, Magnetic flattening of stem-cell spheroids indicates a size-dependent elastocapillary transition, Physical Review Letters **114**, 098105 (2015).

[32] F. Serwane, A. Mongera, P. Rowghanian, D. A. Kealhofer, A. A. Lucio, Z. M. Hockenbery, and O. Campàs, in vivo quantification of spatially varying mechanical properties in developping tissue, Nature Methods **14**, 181 (2017).

[33] P. Marmottant, A. Mgarbel, J. Kafer, B. Audren, J.-P. Rieu, J.-C. Vial, B. V. der Sanden, A. Marée, F. Graner, and H. Delanoe-Ayari, The role of fluctuations and stress on the effective viscosity of cell aggregates, Proceedings of the National Academy of Sciences USA **106**, 17271 (2009).

[34] J. Ranft, M. Basan, J. Elgeti, J.-F. Joanny, J. Prost, and F. Jülicher, Fluidization of tissues by cell division and apoptosis., Proc Natl Acad Sci U S A **107**, 20863 (2010).

[35] G. Charras and A. Yap, Tensile forces and mechanotransduction at cell-cell junctions, Curr Biol **28**, 445 (2018).

[36] K. Bambardekar, R. Clément, O. Blanc, C. Chardes, and L. PF, Direct laser manipulation reveals the mechanics of cell contacts in vivo, Proc Natl Acad Sci **112**, 1416 (2015).

[37] S. Tlili, C. Gay, F. Graner, P. Marcq, F. Molino, and P. Saramito, Mechanical formalisms for tissue dynamics., Eur Phys J E Soft Matter **38**, 121 (2015).

[38] N. Khalilgharibi, J. Fouchard, N. Asadipour, R. Barrientos, M. Duda, A. Bonfanti, A. Yonis, A. Harris, P. Mosaffa, Y. Fujita, A. Kabla, Y. Mao, B. Baum, J. Munoz, M. Miodownik, and G. Charras, Stress relaxation in epithelial monolayers is controlled by the actomyosin cortex, Nat Phys **15**, 839 (2019).

[39] A. Bonfanti, J. Fouchard, N. Khalilgharibi, G. Charras, and A. Kabla, A unified rheological model for cells and cellularised materials, Royal Society Open Science **7**, 190920 (2020).

[40] M. Geerligs, G. W. M. Peters, P. A. J. Ackermans, C. W. J. Oomens, and F. P. T. Baaijens, Linear viscoelastic behavior of subcutaneous adipose tissue., Biorheology **45**, 677 (2008).

[41] S. Nicolle, P. Vezin, and J.-F. Palierne, A strain-hardening bi-power law for the nonlinear behaviour of biological soft tissues, Journal of Biomechanics **43**, 927 (2010).

[42] S. Kaliman, M. Hubert, C. Wollnik, L. Nuic, D. Vurnek, S. Gehrer, J. Lovric, D. Dudziak, F. Rehfeldt, and A.-S.

Smith, Mechanical regulation of epithelial tissue homeostasis, Phys. Rev. X **11**, 031029 (2021).
[43] C. Wilhelm and F. Gazeau, Universal cell labelling with anionic magnetic nanoparticles, Biomaterials **29**, 3161 (2008).
[44] D. Fayol, G. Frasca, C. LeVisage, F. Gazeau, N. Luciani, and C. Wilhelm, Use of magnetic forces to promote stem cell aggregation during differentiation, and cartilage tissue modeling, Adv Mater **25**, 2611 (2013).
[45] J. E. Perez, F. Fage, D. Pereira, A. Abou-Hassan, S. Asnacios, A. Asnacios, and C. Wilhelm, Transient cell stiffening triggered by magnetic nanoparticle exposure, J. Nanobiotechnology **19**, 117 (2021).
[46] A. Nagafuchi, Y. Shirayoshi, K. Okazaki, K. Yasuda, and M. Takeichi, Transformation of cell adhesion properties by exogenously introduced E-cadherin cDNA., Nature **329**, 341 (1987).
[47] W. Goldmann and R. Ezzell, Viscoelasticity in wild-type and vinculin-deficient (5.51) mouse f9 embryonic carcinoma cells examined by atomic force microscopy and rheology, Exp Cell Res **226**, 234 (1996).
[48] O. Thoumine and A. Ott, Time scale dependent viscoelastic and contractile regimes in fibroblasts probed by microplate manipulation., J Cell Sci **110**, 2109 (1997).
[49] N. Desprat, A. Guiroy, and A. Asnacios, Microplates-based rheometer for a single living cell, Rev. Sci. Instrum. **77**, 055111 (2006).
[50] H. Schiessel, R. Metzler, A. Blumen, and T. Nonnenmacher, Generalized viscoelastic models: their fractional equations with solutions, Journal of physics A: Mathematical and General **28**, 6567 (1995).
[51] F. Mainardi, *Fractional calculus and waves in linear viscoelasticity: An introduction to mathematical models* (Imperial College Press, 2010).
[52] A. Berquand, A. Holloschi, M. Trendelenburg, and P. Kioschis, Analysis of cytoskeleton-destabilizing agents by optimized optical navigation and AFM force measurements, Microscopy Today **18**, 34 (2010).
[53] M. Balland, A. Richert, and F. Gallet, The dissipative contribution of myosin ii in the cytoskeleton dynamics of myoblasts, European Biophysics journal **34**, 255 (2005).
[54] E. Zhou, S. Quek, and C. Lim, A power-law rheology-based finite element model for single cell deformation, Biomechanics and modeling in mechanobiology **9**, 563 (2010).
[55] B. Fabry, G. N. Maksym, J. P. Butler, M. Glogauer, D. Navajas, and J. J. Fredberg, Scaling the microrheology of living cells, Phys. Rev. Lett. **87**, 148102 (2001).
[56] L. LeGoff, F. Amblard, and E. M. Furst, Motor-driven dynamics in actin-myosin networks, Physical Review letters **88**, 018101 (2001).
[57] G. Frasca, V. Du, J.-C. Bacri, F. Gazeau, C. Gay, and C. Wilhelm, Magnetically shaped cell aggregates: from granular to contractile materials., Soft Matter **10**, 5045 (2014).
[58] M. Nicolas, P. Duru, and O. Pouliquen, Compaction of a granular material under cyclic shear, Eur. Phys. J. E **3**, 309 (2000).
[59] M. Bouzid, B. Keshavarz, M. Geri, T. Divoux, E. D. Gado, and G. H. McKinley, Computing the linear viscoelastic properties of soft gels using an optimally windowed chirp protocol, Journal of Rheology **62**, 1037 (2018).
[60] M. Geri, B. Keshavarz, T. Divoux, C. Clasen, D. J. Curtis, and G. H. McKinley, Time-resolved mechanical spectroscopy of soft materials via optimally windowed chirps, Physical Review X **8**, 041042 (2018).
[61] P. Kollmannsberger and B. Fabry, Active soft glassy rheology of adherent cells, Soft Matter **5**, 1771 (2009).
[62] G. Erdemci-Tandogan and L. Manning, The cytoplasm of living cells behaves as a poroelastic material., BioXriv (2021).
[63] G. S., L. J., O. L., M. M., S. D.M., R. F., G. P., M. E.W., F. T., X. X., P. S., F. A.W., W. B., H. L.C., B. S., A. B., M. M.L., and K. J.A., Cell and nucleus shape as an indicator of tissue fluidity in carcinoma., Physical Review X **11**, 011033 (2021).
[64] P. Fernandez, L. Heymann, A. Ott, N. Aksel, and P. Pullarkat, Shear rheology of a cell monolayer, New Journal of Physics **9**, 419 (2007).
[65] A. R. Harris, L. Peter, J. Bellis, B. Baum, A. J. Kabla, and G. T. Charras, Characterizing the mechanics of cultured cell monolayers., Proc Natl Acad Sci U S A **109**, 16449 (2012).
[66] G. M., E. A.J., M. S., F. H., J. M.H., M. J.R., F. J.J., G. R.D., and W. D.A., The role of vimentin intermediate filaments in cortical and cytoplasmic mechanics, Biophys. J. **105**, 1562 (2013).
[67] C. Storm, J. J. Pastore, F. MacKintosh, T. Lubensky, and P. A. Janmey, Nonlinear elasticity in biological gels, Nature **435**, 191 (2005).
[68] M. Guo, A. F. Pegoraro, A. Mao, E. H. Zhou, P. R. Arany, Y. Han, D. T. Burnette, M. H. Jensen, K. E. Kasza, J. R. Moore, F. C. Mackintosh, J. J. Fredberg, D. J. Mooney, J. Lippincott-Schwartz, and D. A. Weitz, Cell volume change through water efflux impacts cell stiffness and stem cell fate, Proc. Natl Acad. Sci. USA **114**, E8618 (2017).
[69] P. A. Janmey, D. A. Fletcher, and C. A. Reinhart-King, Stiffness sensing by cells, Physiological reviews **100**, 695 (2020).
[70] P. Fernández and A. Ott, Single cell mechanics: stress stiffening and kinematic hardening., Phys Rev Lett **100**, 238102 (2008).
[71] K. E. Kasza, A. C. Rowat, J. Liu, T. E. Angelini, C. P. Brangwynne, G. H. Koenderink, and D. A. Weitz, The cell as a material, Curr. Opinion Cell Biol. **19**, 101 (2007).
[72] D. A. Fletcher and R. D. Mullins, Cell mechanics and the cytoskeleton, Nature **463**, 485 (2010).
[73] P. Fernandez, P. A. Pullarkat, and A. Ott, A master relation defines the nonlinear viscoelasticity of single fibroblasts, Biophysical Journal **10**, 3796 (2006).
[74] O. Chaudhuri, S. H. Parekh, and D. A. Fletcher, Reversible stress softening of actin networks, Nature **445**, 295 (2007).
[75] N. I. Petridou and C.-P. Heisenberg, Tissue rheology in embryonic organization, EMBO Journal **38** (2019).
[76] A. Boudaoud, A. Burian, D. Borowska-Wykret, M. Uyttewaal, R. Wrzalik, D. Kwiatkowska, and O. Hamant, Fibriltool, an imagej plug-in to quantify fibrillar structures in raw microscopy images, Nature Protocols **9**, 457 (2014).
[77] N. Bufi, P. Durand-Smet, and A. Asnacios, Single-cell mechanics: the parallel plates technique, Methods in cell biology **125**, 187 (2015).
[78] H. Akaike, A new look at the statistical model identification, IEEE Transactions on Automatic Control **19**, 716 (1974).

[79] K. P. Burnham and D. R. Anderson, *Model selection and multimodel inference: a practical information-theoretic approach* (Springer, 2003).

ACKNOWLEDGMENTS

The authors thank O. Cardoso for the assistance he provided on edges tracking. Our thank to A. Fromain for help on VSM measurements and the staff of MPBT (Low temperatures magnetic measurements plateform) for assistance. We thank Ali Abou-Hassan (PHENIX, UMR 8234, Paris) for providing us with the magnetic nanoparticles. The authors gratefully acknowledge funding from the city of Paris Research Program Emergence (Grant IDs 'MAGIC') and support from the European Union (ERC-2014-CoG project MaTissE 648779). The study was partially supported by the Labex Who Am I?, Labex ANR-11-LABX-0071, and the Université de Paris, Idex ANR-18-IDEX-0001 funded by the French Government through its Investments for the Future program.

AUTHOR CONTRIBUTION

F.M., J-C.B., S.A., A.A., C.G., P.M., C.W and M.R. conceived the idea; G.M., F.M., F.F., I.N., L.D., S.A., A.A., and M.R. performed the experiments; V.N., C.G. and P.M. run the parametric inference experiments. S.A., A.A, C.G., P.M. and M.R. analyzed the experiments. S.A., A.A., C.G., P.M., C.W. and M.R. supervised the study. F.M.,S.A., A.A., C.G., P.M. and M.R. wrote the manuscript. G.M., F.M., V.N., F.F., I.N., L.D., S.A., A.A., C.G., P.M., C.W. and M.R. proofread the manuscript.

Appendix A: Methods

Nanoparticles and reagents

The nanoparticles used to magnetically label the F9 cells are citrated iron oxide maghemite (Fe_2O_3) superparamagnetic nanoparticles with a characteristic diameter $\delta_0 \simeq 7-8$ nm (polydispersity 28 %, standard deviation $s \simeq 2$ñm). The magnetization curve (Figure 8) is described by a Langevin function weighted by the nanoparticles size δ:

$$\frac{M(|B|)}{M_{\rm sat}} = \phi(|B|) = \int M^{\rm np}(\delta)\,\mathcal{L}(\xi(\delta))\,P(\delta)\,{\rm d}\delta \qquad \text{(A1)}$$

where $M^{\rm np}$ is the magnetization at saturation of a maghemite nanoparticle, $\xi(\delta) = \mu_0 H M^{\rm np}(\delta)/(k_B T)$ and $\mathcal{L}(x) = \coth(x) - 1/x$. The size distribution P is approximated by a log-normal law with the characteristic diameter δ_0 and the standard deviation s. As particles are superparamagnetic, M is independent of the direction of the magnetic field and applied forces are pulling ones.

We used two different cell types. F9 WT cells were purchased from ATCC. CT26 cells were purchased from ATCC. To inhibit actin filament formation, Latrunculin A (1 μM) purchased from Sigma (L5163) is used in some experiments during aggregate formation and stimulation. (+/-)-Blebbistatin (203390, Sigma-Aldrich) is added at 10 μM to inhibit myosin activity in dedicated experiments. EGTA (0.4 mM) may be added at the same stage to act as a calcium chelator and decrease cell-cell cadherin mediated interactions as well as individual calcium influx.

Immunofluorescence was performed using SiR-actin (2 μM for 1 hour) to stain actin filaments and DAPI to label nuclei. E-cadherin antibody (ECCD-2 from Thermofisher used at 1 : 50 for 2 hours) coupled with a secondary anti-rat GFP antibody is used to enhance this cell-cell adhesion molecule. Cleaved Caspase-3 antibody (Cell Signal) was used to check for possible apoptosis in multicellular aggregates.

Cryosections

Multicellular aggregates were fixed in 4% PFA for 1 hour at room temperature then embedded in OCT (Optimal Cutting Compound, 361603E, VWR). After freezing in isopentane cooled down in liquid nitrogen, samples were kept at $-20°C$. $6-10\,\mu$m thick cryosections were obtained (Leica CM1520). Fibriltool ImageJ plugin [76] was used to quantitatively analyzed the length of the cortical actin filaments or the organization of cell-cell adhesion.

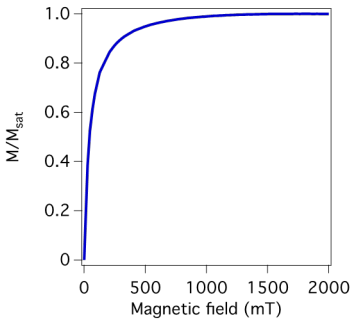

FIG. S8: **Magnetization curve of the iron oxide nanoparticles.** The magnetization normalized by the saturation magnetization is plotted as a function of the external magnetic field.

Magnetic cell labeling and magnetic formation of multicellular aggregates

F9 murine cells are grown in DMEM supplemented with 5 % fetal bovine serum (FBS) and 1 % antibiotics (penicillin/streptomycin) at 37°C and 5 % CO_2. When cells are at confluence, nanoparticles solution ([Fe] = 2 mM in RPMI) is added for 2 h. Nanoparticles are internalized in cells through endocytosis pathways and are finally localized within intracellular vesicles identified as endosomes [43]. At high doses (50 mM), transient aggregation of endosomes at the cell membrane may cause transient modification of actin network while cytoskeleton is not modified at low doses (5 mM) [45]. The 2 mM incubation concentration thus guaranties the integrity of the cytoskeleton network and function. After incubation, cells are washed with fresh RPMI and detached with trypsin to be seeded in 2 % agarose gel cylindrical molds (diameter 2 mm, height 1.5 mm) or cubic molds 1 mm square) obtained by forming a network of small magnetic cylinders (or cubes) within an agarose mold (Figure 9). Indeed by removing the magnets below, and taking off the magnetic cylinders or cubes within the gel, we achieve to have wells to seed cells within. The seeding of cells (1 million) in the wells is then magnetically driven by the magnets below the dish (Figure 9). Cell-cell contacts develop overnight to produce a cohesive cylindrical tissue that can be removed from the mold (Figure 1a-d). The resulting aggregates are removed from the well after 16 h (overnight maturation), showing important cell-cell adhesions. Their size is reproducible: cylindrical aggregates of 2 mm diameter and 0.8 mm height for 10^6 cells and cuboidal aggregates of 1 mm square base and *circa* 0.6 mm height for $2.5\,10^5$ cells . In addition, magnetic molding allows us to form multicellular aggregates in presence of chosen inhibitors. The resulting aggregates (Figure 1a-e) have a homogeneous bulk saturation magnetization ($M_V^{\mathrm{sat}} = 103 \pm 16\,\mathrm{A.m^{-1}}$) measured with a vibrating sample magnetometer (Quantum Design, Versalab). Cell viability in presence of magnetic nanoparticles was characterized on cell culture with Alamar blue dyes (Invitrogen). To assess the potential harmfulness of the magnetic labelling on suspended cells, we compared during three days the survival rate of cells with or without magnetic nanoparticles and submitted some magnetically labelled cells to magnetic field (Figure 10). No cytotoxicity is noticed even in presence of magnetic field.

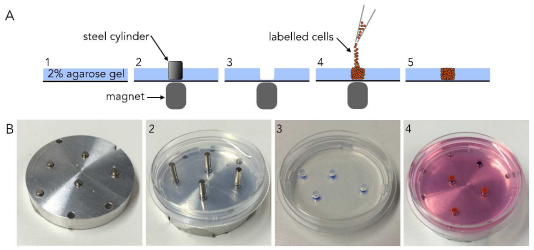

FIG. S9: **Magnetic molding of cylindrical multicellular spheroids. a** Schematic representation and **b** pictures of the different steps of the molding protocol. (1) A layer of 2% agarose solution in PBS is poured into a culture dish. (2) A cylindrical permanent magnet is placed under the dish while the agarose is still liquid to attract a calibrated steel cylinder (2 mm in diameter). (3) The agarose solidifies as it cools down and the cylinder is removed to form a cylindrical mold. (4) The dish is filled with DMEM medium without FBS and magnetically labeled cells are seeded in the wells. The magnet attracts and compacts the cells for 30 seconds before being removed. (5) The dish is incubated at 37°C and 5% CO_2 overnight to allow tissue formation.

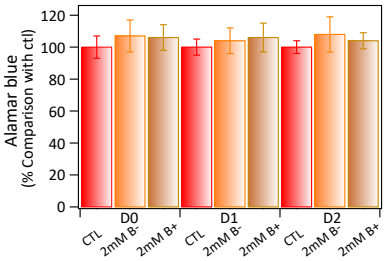

FIG. S10: **Cytotoxicity of the nanoparticles on F9 cells** Viability of magnetically labelled cells is estimated from the difference in fluorescence intensity level of Alamar blue compared with unlabelled cells. Labelled cells are either not submitted to magnetic field (B- condition) or submitted to a 100 s long maximal magnetic field for 10 times a day. Results are obtained from 3 independent experiments. No differences are noticeable between the three conditions, promoting the cytosafety of the iron oxyde nanoparticles on F9 cells for 3 days.

Magnetic field applicator

The magnetic field used to deform the magnetized aggregate was generated with an electromagnet composed of a custom-made water-cooled coil (6 Ω, 14 mH) wrapped around a soft iron polar piece (diameter 55 mm, height 85 mm) allowing the passage of a current up to 10A. In its upper part, the diameter of the polar piece goes down from 55 mm to 5 mm. The top of the polar piece was 3 mm below the center of the aggregate. The electromagnet tension was controlled with a TGA 1242 signal generator (Aim&TTi) and amplifier (Kebco BOP).

The shape of the polar piece was optimized to maximize the magnitude of the magnetic field gradient $\mathrm{d}B/\mathrm{d}z$ along the z coordinate ($30\mathrm{T.m^{-1}}$ when the magnetic field reaches its maximum value 120 mT) as well as its homogeneity in the aggregate volume. Nanoparticles magnetize in the presence of the magnetic field B. As a result, the aggregate displays a magnetization

$M_V = M_V^{\rm sat}\,\phi(B/B^{\rm sat})$ per unit volume (for ϕ, $M_V^{\rm sat}$ and $B^{\rm sat}$, see above). The magnetic field generated at the center of the aggregate linearly depends on the applied tension (see Figure 11a) and the magnetic field gradient was almost homogeneous (less than 20 % variation over a size exceeding one millimeter), whatever the applied tension (Figure 11b) ensuring a homogenous force on cells.

The set up was calibrated and characterized in order to determine the bulk flattening magnetic force generated as a function of the applied tension $V(t)$ using the set-up as a tensiometer [31]. Ferrofluid drops (aqueous solution of the nanoparticles used for cell labelling) of various size deposited on a superhydrophobic surface in a silicon bath, were flattened. Fitting each experimental profile with the Laplace equation for capillarity in non-wetting conditions provided the surface tension. This measurement was validated by comparison with classic sessile drop experiment (Figure 11c). The maximum value of the magnetic force density was measured to be close to $2.5\,{\rm kN.m^{-3}}$.

Signal generation and synchronization

The tension signal is transferred to the generator using the Waveform Manager Plus software. To synchronize the deformation signal with the force generation, a LED, powered by a pulse generator that is synchronized with the signal generator, was used to overexpose a single image of the movie at the beginning of the deformation sequence.

Image analysis

The displacement $\delta h(t)$ of the upper aggregate surface is recorded by fast camera imaging and quantified through image analysis. The threshold of detection in displacement is of the order of $0.5\,\mu$m while the overall aggregate strain $\varepsilon \equiv \delta h/h_0$ (positive with the conventions used) does not exceed 5%(*i.e.*, $\delta h \leq 50\,\mu$m). Deformations were analyzed using the image correlation based tracking algorithm on ImageJ: Tracker Install (developped by Olivier Cardoso `sites.google.com/site/oliviercardoso/Home/plugins`). It extracts the displacement of the aggregate upper interface as a function of time ($\delta h(t)$ in Figure 1f-h). Vibrations of the setup (mainly due to the water circulation use to thermalize the container) were compensated by tracking a fixed point on the container bottom (adsorbed dust for instance) and subtracting its motion from the interface displacement. The precision on the interface displacement is $\pm 0.5\,\mu$m. Sampling frequencies are between 10 to 100 Hz depending on the experiments.

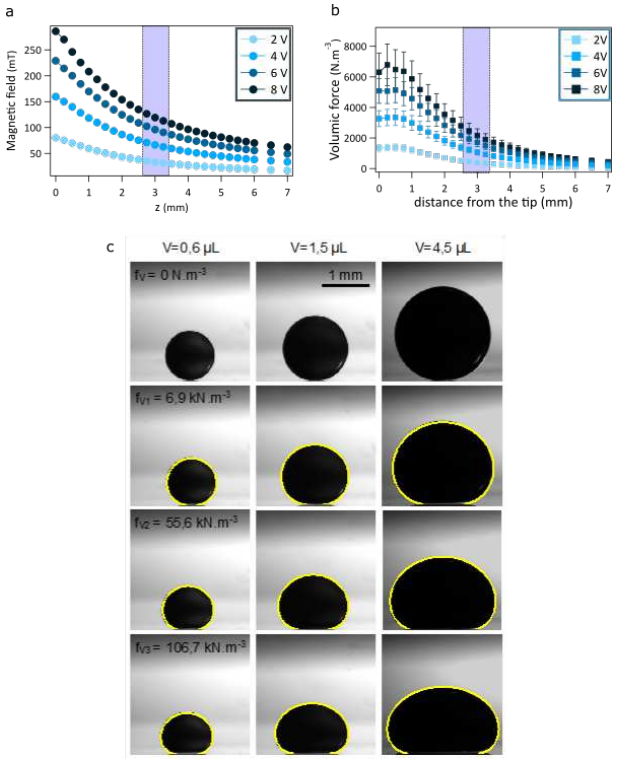

FIG. S11: **Calibration of the magnetic field generator. a** Magnetic field created by the electromagnet as a function of the distance to the top of the polar piece for different tensions applied to the amplifier. The center of the aggregate is 3 mm above the electromagnet so the aggregate position is emphasized in violet. **b** Force per unit volume extracted from the measured magnetic field and aggregate magnetization curve. **c** Ferrofluid drops ([Fe]=1.25 M) of three different volumes ($0.6, 1.5, 4.5\,\mu$L) deposited on a superhydrophobic coated glass surface, in a silicon oil bath, are submitted to increasing magnetic flattening forces (under normal gravity, $f_{V1} = 6.9\,{\rm kN.m^{-3}}$, $f_{V2} = 56\,{\rm kN.m^{-3}}$, $f_{V3} = 107\,{\rm kN.m^{-3}}$) corresponding to increasing tensions applied to the amplifier (respectively: $0, 1.2, 4.8, 8$ V). Droplets experimental equilibrium profiles are fitted with theoretical capillary profile (yellow), obtained by integrating numerically the Laplace equation for capillarity in non-wetting conditions (using Matlab's function ode45).

Microplate rheometer

A microplate rheometer was used both for single cell and for aggregate measurements [49]. In such a device, the sample is compressed between two parallel microplates. One is rigid. The other is flexible. Its deflection δ is related to the force $F = k\delta$ applied to the sample through the calibrated stiffness k.

However, since the set-up was initially designed to test single cells (size around $10\,\mu$m), the flexible microplate

had to be adapted to both the size (500 μm) and the stiffness of cell aggregates. Thus, new spatula-like plates have been created with wide tips (1 mm in width) and a thin neck (around 5 mm long and 100 μm width) to be able to test large but very soft objects like cell aggregates. The stiffness of the spatula was 27.8 nN/μm. For single cell measurements, as F9 cells are very soft, we used a microplate of 0.6 nN/μm. The flexible microplates were otained by heating and pulling borosilicate plates of 10 cm x 1 mm x 200 μm [77]. The stiffness of the flexible microplates was calibrated using a standard microplate itself calibrated following the protocol detailed in [49]. The setup was mounted on a Leica DMIRB inverted microscope (Leica Microsystems, Rueil-Malmaison, France), and samples were visualized using a x10 objective for aggregates and a x63 objective for single cell measurements. The stress σ applied to the sample was defined as the the force $F = k\delta$ divided by the contact area A between the sample and the plate: $\sigma = F/A$. For single cells, the contact areas between the plates and the cell were estimated by assuming a circular contact, i.e. $A = \pi D^2/4$. The apparent contact diameters D_F and D_R (respectively for the flexible and rigid plates) were measured on bright field images. Since D_F and D_R are usually different, we retained their mean square value, leading to $\sigma = \frac{8F}{\pi(D_F^2+D_R^2)}$. As for the cuboid cell aggregates of dimensions $L \times L \times h$, they initially lie on their square face. They are seized laterally between both microplates (Figure 3c). Hence, the contact surface is rectangular and its area $A = Lh$ is determined through bright field imaging. L is measured directly during the experiment. It may slightly differ from the measurement obtained before the microplate handling. h is estimated by using images taken before the microplates grasped the aggregates: a correction is applied to take into account the possible deformation due to handling (it is computed from the corresponding L values). Finally, the uniaxial cell or aggregate strain perpendicular to plates was defined as $\varepsilon = \frac{L-L_0}{L_0}$, where L_0 (resp. L) is the distance between the parallel microplates before (resp. after) compression. The apparent modulus is then given by $E = \sigma/\varepsilon$. Dynamical measurements were carried out in the frequency range from 0.1 to 3.2 Hz for cell aggregates, and from 0.1 to 0.4 Hz for single cells. In the latter case, measurements at higher frequencies were difficult to analyze: the very low stiffness of the flexible plate (at the limit of the technique), required to measure the very low viscoelastic modulus of F9 cells, makes it very sensitive to all viscous flows induced by the plate motion in the complex geometry around the plates and between both plates around the aggregate.

Broad spectrum signal

The stress signal we applied for the broad spectrum method is a superposition of several sinusoidal signals:

$$\sigma(t) = \sigma_0\, \varphi(t) \sum_{i=1}^{n} \rho_i \cos(2\pi\, f_i\, t + \phi_i), \qquad \text{(A2)}$$

where σ_0 is used to tune the amplitude and $\varphi(t) = \tanh(\lambda t)$ is an envelope function used to smooth the beginning of the signal over the first few seconds. The frequency range is chosen as 0.1-10 Hz. The $n = 32$ frequencies f_i are equally spaced logarithmically within this range. The phases ϕ_i are chosen randomly within $[0, 2\pi]$. In order to damp high frequencies, the magnitude of the real prefactor ρ_i is chosen to decrease with the frequency. More precisely, ρ_i^2 is drawn uniformly within $[0, f_{\min}^2/f_i^2]$, which ensures that the complex amplitude $\rho_i\, e^{i\,\phi_i}$ is distributed uniformly in the disk of radius $f_{\min}/f_i$, a scaling reminiscent of $1/f$ noise. We give in Supp. Fig.12 the Fourier transform of both the signal, see Eq. (A2), and the aggregate response. By analysing the signal at null-stress, we estimate the noise level of the height measurement to 10^{-3}, comfortably below the amplitude 10^{-1} of the highest frequency involved.

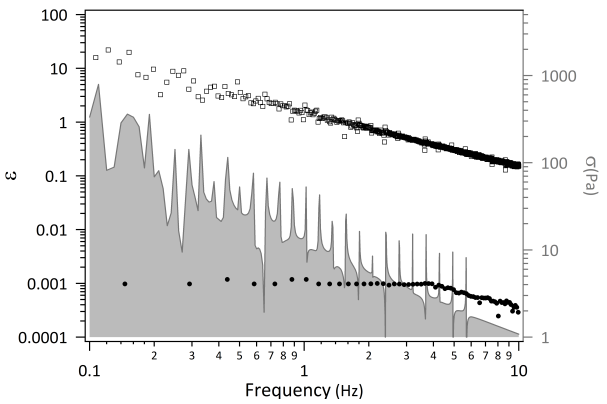

FIG. S12: **Fourier analysis of the broad spectrum signal and response.** Curve with grey shadow: Fourier transforms of the stress signal, which displays clearly the $N = 32$ frequencies chosen with the $1/f$ scaling for their respective amplitudes. Empty squares: Fourier transform of the strain response of the F9 multicellular aggregate. Filled circles: for comparison, estimation of the noise level for the strain measurement in the experimental setup. This noise estimation is taken as the strain difference with the power-law response to a $\sigma = 1.1$ Pa step.

Rheological models

Generally speaking, a rheological model may be defined by a p-dimensional parameter vector $\vec{\theta}$ and by an equation of the form $\varepsilon_{\rm loc}(t) = \mathcal{R}(\{\sigma_{\rm loc}(t')\}_{t'\leq t}, \vec{\theta})$, where

Model	AIC ($\times 10^4$)	α	$J\,(\mathrm{Pa}^{-1})$	$a\,(\mathrm{Pa}^{-1})$	$\bar{a}\,(\mathrm{Pa}^{-2})$	$b\,(\mathrm{Pa}^{-1})$	β
(A4)	$\mathbf{-5.69 \pm 0.06}$	0.25 ± 0.02	0.045 ± 0.010	$\times$	$\times$	$\times$	$\times$
(A5)	$\mathbf{-7.20 \pm 0.07}$	0.22 ± 0.01	0.13 ± 0.03	2.2 ± 0.5	$\times$	$\times$	$\times$
(A6)	-6.73 ± 0.07	0.22 ± 0.02	0.07 ± 0.02	$\times$	0.7 ± 0.4	$\times$	$\times$
(A7)	-6.78 ± 0.07	0.22 ± 0.01	0.08 ± 0.01	$\times$	$\times$	-0.47 ± 0.15	$\times$
(A8)	-7.16 ± 0.08	0.22 ± 0.01	0.16 ± 0.08	3.4 ± 3.3	-0.6 ± 1.0	-0.1 ± 0.4	$\times$
(A9)	$\mathbf{-8.30 \pm 0.05}$	0.29 ± 0.02	0.07 ± 0.01	0.5 ± 0.2	$\times$	$\times$	0.20 ± 0.06

TABLE I: **Model selection.** The AIC and optimized parameter values are given for models (A4-A9) (mean $\pm$ standard deviation, $N = 8$).

$\mathcal{R}$ is an integro-differential operator acting on the function $\sigma_{\mathrm{loc}}(t)$.

The rheological models we considered, defined in the following paragraphs by order of increasing complexity, contain fractional integrals [51], defined as:

$$I^{\tau}_{\alpha}(f) = \frac{1}{\tau^{\alpha}\,\Gamma(\alpha)} \int_0^t (t-t')^{\alpha-1} f(t')\,\mathrm{d}t'\,. \tag{A3}$$

where an arbitrary time scale τ is set to $\tau = 1$ s and where $I^{\tau}_{\alpha}(f)$ has the same dimension as f.

a. Linear fractional rheology This model has two parameters (both positive):

$$\varepsilon_{\mathrm{loc}} = J_1\; I^{\tau}_{\alpha}(\sigma_{\mathrm{loc}}) \qquad \vec{\theta} = (\alpha, J_1) \tag{A4}$$

where α is dimensionless and J_1 is in Pa^{-1}.

b. Nonlinear fractional rheology These are nonlinear versions of the order $\alpha \geq 0$ fractional rheology:

$$\varepsilon_{\mathrm{loc}} = J_1\; I^{\tau}_{\alpha}\left(\frac{\sigma_{\mathrm{loc}}}{1 + a\,\sigma_{\mathrm{loc}}}\right) \qquad \vec{\theta} = (\alpha, J_1, a) \tag{A5}$$

$$\varepsilon_{\mathrm{loc}} = J_1\; I^{\tau}_{\alpha}\left(\frac{\sigma_{\mathrm{loc}}}{1 + \bar{a}\,\sigma^2_{\mathrm{loc}}}\right) \qquad \vec{\theta} = (\alpha, J_1, \bar{a}) \tag{A6}$$

$$\varepsilon_{\mathrm{loc}} = J_1\; I^{\tau}_{\alpha}\left(\sigma_{\mathrm{loc}}(1 + b\,\sigma_{\mathrm{loc}})\right) \qquad \vec{\theta} = (\alpha, J_1, b) \tag{A7}$$

$$\varepsilon_{\mathrm{loc}} = J_1\; I^{\tau}_{\alpha}\left(\frac{\sigma_{\mathrm{loc}}(1 + b\,\sigma_{\mathrm{loc}})}{1 + a\,\sigma_{\mathrm{loc}} + \bar{a}\,\sigma^2_{\mathrm{loc}}}\right) \qquad \vec{\theta} = (\alpha, J_1, a, \bar{a}, b) \tag{A8}$$

where a and b are in Pa^{-1} and $\bar{a}$ is in Pa^{-2}. These models give various functional forms to the nonlinear relationship between the fractional derivative $I^{\tau}_{-\alpha}(\varepsilon_{\mathrm{loc}})$ and σ_{loc}. By construction, they all reduce to (A4) when $a = \bar{a} = b = 0$.

c. Nonlinear fractional rheology, two fractional integrals (orders $\alpha \geq \beta \geq 0$)

$$\varepsilon_{\mathrm{loc}} = J_2\; I^{\tau}_{\alpha-\beta}\left(\frac{\Sigma_{\mathrm{loc}}}{1 + a\,\Sigma_{\mathrm{loc}}}\right) \qquad \vec{\theta} = (\alpha, \beta, J_2, a), \tag{A9}$$

where we define $\Sigma_{\mathrm{loc}} = I^{\tau}_{\beta}(\sigma_{\mathrm{loc}})$, which reduces to $\Sigma_{\mathrm{loc}} = \sigma_{\mathrm{loc}}$ in the limit where $\beta = 0$. This model reduces to (A5) when $\beta = 0$, and to (A4) when $a = 0$.

d. Stress-strain relationship The volumic nature of the applied magnetic force implies that the stress is not uniform within the samples. Rather, it increases approximately linearly from the free surface of the aggregate up to its maximum value at the substrate surface: $\sigma_{\mathrm{loc}}(z) = \sigma_{\max}\,(1 - z/h_0) = 2\sigma\,u$, where σ is the spatially averaged applied stress and $u = 1 - z/h_0$ is the reduced distance from the upper surface of the aggregate. As a result, the local deformation $\varepsilon_{\mathrm{loc}}$ also depends on altitude *via* the (nonlinear) differential equation $\varepsilon_{\mathrm{loc}}(z,t) = \mathcal{R}\left(\{\sigma(z,t')\}_{t'\leq t}, \vec{\theta}\right)$. Correspondingly, the overall aggregate deformation can be obtained by averaging the local deformation field. For a response $\mathcal{R}$ and a homogeneous magnetic force f_V, the macroscopic strain is given by:

$$\varepsilon(t) = \langle \varepsilon_{\mathrm{loc}}(z,t)\rangle_z = \langle \mathcal{R}\left(\{2u\,\sigma(t')\}_{t'\leq t}\right)\rangle_{0\leq u\leq 1}\,. \tag{A10}$$

When the rheology $\mathcal{R}$ is linear, the spatial average commutes with $\mathcal{R}$, and global variables are also related through the same operator: $\varepsilon(t) = \mathcal{R}\left(\{\sigma(t')\}_{t'\leq t}, \vec{\theta}\right)$. For instance, for the linear fractional constitutive equation (A4) one also has $\varepsilon = J_1\; I^{\tau}_{\alpha}(\sigma)$ and for a step stress of magnitude σ_0, using Eq. (A3) we find a power law response:

$$\varepsilon(t) = \sigma_0\,\frac{J_1}{\Gamma(1+\alpha)}\left(\frac{t}{\tau}\right)^{\alpha}\,. \tag{A11}$$

Comparing this result with definition (1), we obtain the creep compliance $J_0^{\mathrm{L}} = J_1/\Gamma(1+\alpha)$ for the linear case.

More care needs to be exercised when the rheology $\mathcal{R}$ is nonlinear. A useful example is the case of Model (A5), for which the expected overall deformation reads:

$$\begin{aligned}\varepsilon(t) &= \int_{u=0}^{u=1} J_1\; I^{\tau}_{\alpha}\left(\frac{2u\sigma(t)}{1+2au\sigma(t)}\right)\mathrm{d}u \\ &= J_1\; I^{\tau}_{\alpha}\left(\int_{u=0}^{u=1}\frac{2u\sigma(t)}{1+2au\sigma(t)}\,\mathrm{d}u\right) \\ &= J_1\; I^{\tau}_{\alpha}\left(\frac{2a\sigma(t) - \log(1+2a\,\sigma(t))}{2a^2\sigma(t)}\right)\,.\end{aligned}$$

For a step stress, the compliance now depends on the step magnitude σ_0 in this non-linear case (see Figure 5e):

$$J_0^{\mathrm{NL}} = \frac{J_1}{\Gamma(1+\alpha)}\,\frac{2a\sigma_0 - \log(1+2a\,\sigma_0)}{2a^2\sigma_0^2}.$$

Parametric inference

In order to assess to what degree the rheological model, defined by $\mathcal{R}$, is suitable to describe the experimental data $\{\varepsilon_{\exp}(t)\}_t$, we assume that the experimental noise $\phi(t)$ is white and Gaussian (amplitude s) and contributes additively within the measured deformation value:

$$\varepsilon_{\exp}(t) = \mathcal{R}(\{\sigma(t')\}_{t'\leq t}, \vec{\theta}) + \phi(t)\,.$$

We then determine the values of the parameters $\vec{\theta}$ and s, *i.e.*, $p+1$ real numbers, that maximize the likelihood function

$$L\left(\{\varepsilon_{\exp}(t)\}_t \,\middle|\, \{\sigma(t)\}_t, \vec{\theta}\right) = \frac{1}{(2\pi s^2)^{N_t/2}} \exp\left(-\sum_{t=1}^{N_t} \frac{\|\varepsilon_{\exp}(t) - \mathcal{R}(\{\sigma(t')\}_{t'\leq t}, \vec{\theta})\|^2}{2s^2}\right) \tag{A12}$$

for N_t time points (typically $N_t \simeq 7\,10^3$ here). Indeed, the likelihood L indicates how likely it is to observe the actual experimental data $\{\varepsilon_{\exp}(t)\}$, given the rheological model (encoded in $\mathcal{R}$), the parameter set $(\vec{\theta}, s)$ and the imposed stress history $\{\sigma(t)\}$. The larger the likelihood, the better the model and its parameters fit the experimental data.

Model selection

The rheological models defined by Eqs. (A4-A9) are tested against the experimental data by maximizing the likelihood function (A12), yielding optimal parameters. Table I gathers the average values and standard deviations of these optimal parameters ($N = 8$).

Once the parameter values of each model have been optimized, we need to be able to select the best model. One difficulty is that the various models contain different numbers of parameters. In order to avoid both too simple models and too complex models (since overfitting may reduce reproducibility and/or predictability), we compute for each model the Akaike information criterion [78] defined as

$$\mathrm{AIC} = -2\log L + 2(p+1)\,. \tag{A13}$$

The AIC provides an objective estimation of the quality of each model, penalizing the number of parameters p and favouring a high value of the likelihood function L [79]:

$$\mathrm{AIC}(\mathcal{R}) = \sum_t \frac{\|\varepsilon_{\exp}(t) - \mathcal{R}(\{\sigma(t')\}_{t'}, \vec{\theta})\|^2}{s^2} + N_t \log(2\pi s^2) + 2(p+1) \tag{A14}$$

The absolute AIC values are not particularly meaningful, but their relative values provide a comparison between the different models, where the best model corresponds to the lowest AIC value.

On Figure 4b, the experimentally measured deformation $\varepsilon(t)$ (black points) is compared with the predictions provided by the linear fractional model (A4) and the non-linear fractional models (A5) given the applied stress $\sigma(t)$ displayed on Figure 4a. The linear fractional model (A4) fails to reproduce the time evolution of the measured deformation, while the non-linear fractional model (A5) yields satisfactory predictions. Inspection of Table 1 shows that estimated AIC values agree with these qualitative observations. Further, all nonlinear fractional models (A5-A7) have a lower AIC than that of the linear fractional model (A4). Among (A5-A7) the lowest AIC is obtained by (A5). The AIC obtained for (A5) is consistent with that of the more complex model (A8); however most parameter values obtained for (A8) are consistent with zero. For these reasons, we designate (A5) as the best fractional model with one fractional integral.

Finally, introducing a second fractional order in model (A9) allows to predict almost perfectly the deformation history (Supplemental material). The relevance of this model is confirmed by comparing phase space plots. However, numerical integration shows that the power-law behavior then predicted for step stress assays is characterized by an exponent that depends on the stress amplitude σ_0, at variance with experimental observations. Further, the model fails to reproduce quantitatively the σ_0 dependence of the creep compliance J_0 (Supplemental material).